



저작자표시-비영리-변경금지 2.0 대한민국

이용자는 아래의 조건을 따르는 경우에 한하여 자유롭게

- 이 저작물을 복제, 배포, 전송, 전시, 공연 및 방송할 수 있습니다.

다음과 같은 조건을 따라야 합니다:



저작자표시. 귀하는 원저작자를 표시하여야 합니다.



비영리. 귀하는 이 저작물을 영리 목적으로 이용할 수 없습니다.



변경금지. 귀하는 이 저작물을 개작, 변형 또는 가공할 수 없습니다.

- 귀하는, 이 저작물의 재이용이나 배포의 경우, 이 저작물에 적용된 이용허락조건을 명확하게 나타내어야 합니다.
- 저작권자로부터 별도의 허가를 받으면 이러한 조건들은 적용되지 않습니다.

저작권법에 따른 이용자의 권리는 위의 내용에 의하여 영향을 받지 않습니다.

이것은 [이용허락규약\(Legal Code\)](#)을 이해하기 쉽게 요약한 것입니다.

[Disclaimer](#)

Ph.D. Thesis

**Doppler parameter estimation from SAR (Synthetic
Aperture Radar) for velocity measurements:
Sea surface current and ship velocity**

속도 측정을 위한 SAR 도플러 파라미터 추출: 표층 해류와 선박 속도

Ki-mook Kang

Aug 2018

Major in Satellite Geophysics

School of Earth and Environmental Sciences

Graduate School

Seoul National University

이학박사 학위논문

**Doppler parameter estimation from SAR (Synthetic
Aperture Radar) for velocity measurements:
Sea surface current and ship velocity**

속도 측정을 위한 SAR 도플러 파라미터 추출: 표층 해류와 선박 속도

강 기 목

2018년 8월

서울대학교 대학원

지구환경과학부

인공위성지구물리 전공

Doppler parameter estimation from SAR (Synthetic
Aperture Radar) for velocity measurements:
Sea surface current and ship velocity

속도 측정을 위한 SAR 도플러 파라미터 추출: 표층 해류와 선박 속도

지도교수 김 덕 진

이 논문을 이학박사 학위논문으로 제출함

2018년 8월

서울대학교 대학원

지구환경과학부

강 기 목

강기목의 이학박사 학위논문을 인준함

2018년 8월

위 원 장 _____ 조 양 기 (인)

부위원장 _____ 김 덕 진 (인)

위 원 _____ 남 성 현 (인)

위 원 _____ 박 상 은 (인)

위 원 _____ 이 우 경 (인)

Abstract

Doppler parameter from SAR (Synthetic Aperture Radar) is among the most effective tools for velocity measurements. The physical principle for estimating radial velocity utilizes the Doppler shift extracted from SAR data. The Doppler shift is caused by the relative motion between a sensor and target. The Doppler parameter can be used as an important source for velocity measurements in various applications including oceanography, geology, civilian, and military fields. Based on the type of SAR products and Doppler parameter estimation techniques, specific applications including distributed and artificial moving target velocities can be estimated with the velocity range. In this thesis, I examined a distributed target velocity, a sea surface current, using SAR raw data and an artificial target velocity, a ship, using SAR SLC data of a single channel SAR system.

First, the Doppler parameter in the received radar signal from the SAR raw data was used to retrieve the sea surface velocity. Sea surface velocity is derived by calculating Doppler shift anomalies between predicted and estimated Doppler centroids. The predicted Doppler centroid is defined as the Doppler centroid, in which it is assumed that the target does not move, and it is calculated based on improved geometric parameters of a satellite including the satellite's orbit, beam pointing direction, and attitude with respect to the rotations of Earth. I used an established model with improved parameters (including slant range distance, look angle, and hour angle) and

an iterative fitting procedure. The fitting procedure included a global fitting method and an attitude control algorithm for correct biases. The estimated Doppler shift that represents the actual Doppler centroid in the situation of real SAR data acquisition can be directly extracted from ScanSAR raw signal data calculated by applying the adjusted Average Cross Correlation Coefficient (ACCC). The characteristics of sea surface velocities under hurricane conditions were investigated using RADARSAT-1 ScanSAR Doppler centroid measurements. Five different hurricanes (i.e., Typhoon Xangsane, Hurricane Dean, Hurricane Ivan, Hurricane Lili, and Hurricane Kyle) and sequential acquisitions of two cases (Hurricane Lili and Hurricane Kyle) were selected to investigate the contribution of wind-induced waves to Doppler velocities and compared to in-situ measurements of drifting buoys. The results indicate that hurricane-generated seas and associated winds and waves appear to differ from those of the ordinary sea state. This leads to lower estimates of Doppler velocities than the expected estimates and that are significantly closer to the sea surface current velocities. In this respect, our study is the first attempt to characterize Doppler velocities influenced by tropical cyclones using different and sequential RADARSAT-1 ScanSAR data.

Second, we investigated the potential for automatic calculation of ship velocity using the azimuth offset between ship and wake in SAR SLC imagery. The azimuth offset between ship and wake is proportional to the Doppler shift effect of the back-scattered signal, and is thus related to the radial velocity of the moving target. Our methods automatically identified ships and wakes from TanDEM-X SLC images

using convolutional neural networks (CNN), a deep learning technique. An accurate reference point between the ships and wakes was identified using Radon transforms and edge filtering. Additionally, ship velocity was estimated using the along-track interferometry (ATI) phase due to the Doppler shift effect. Using the Korea Strait as a test site estimating moving ship velocity using TanDEM-X data, we compared the accuracy of the ship and wake detection rate with Automatic Identification System (AIS) data. We also compared the processing results from the azimuth offset to those from the ATI and in-situ measurements of AIS to determine the feasibility of estimating moving target velocity.

Thus, the estimation of a Doppler parameter, such as Doppler centroid measurements, azimuth offset, and ATI, can lead to the effective extraction of velocity in various applications including sea surface current and ship velocity.

Keywords – Synthetic aperture radar (SAR), Doppler centroid measurements, azimuth offset, sea surface current, ship velocity, along-track interferometry (ATI) SAR

Student Number: 2012-30890

List of Contents

1	Introduction.....	- 1 -
1.1	Overview.....	- 1 -
1.2	Background of Doppler parameter from SAR.....	- 6 -
1.3	Objectives	- 15 -
2	Retrieval of sea surface velocity during tropical cyclones using RADARSAT-1 ScanSAR Doppler centroid measurements	- 17 -
2.1	Background	- 17 -
2.2	Data set and meteorology.....	- 21 -
2.3	Method.....	- 30 -
2.3.1	Predicted Doppler centroid.....	- 30 -
2.3.2	Estimated Doppler centroid.....	- 37 -
2.3.3	Extraction of Sea surface velocity from Doppler shift.....	- 40 -
2.4	Result and discussion	- 43 -
3	Retrieval of ship velocity using azimuth offset from TanDEM-X SLC data-	62
-		
3.1	Background	- 62 -
3.2	Study area and data acquisition.....	- 66 -
3.3	Method.....	- 71 -
3.3.1	Azimuth offset calculated from Radon transform	- 73 -
3.3.2	Along-track interferometry.....	- 78 -

3.4	Result and discussion	- 81 -
4	Conclusion	- 91 -
	Appendix A. Detailed derivation of Doppler velocity during tropical cyclones-	94 -
	Appendix B. Convolutional neural networks for detecting ship and wake using SAR SLC data	- 100 -
	References	- 106 -
	국문 요약	- 116 -

List of figures

Figure 1-1 Overview of Doppler parameter estimation from SAR for velocity measurements - 4 -

Figure 1-2 Doppler parameter estimator - 5 -

Figure 1-3 SAR geometry - 7 -

Figure 1-4 SAR geometry in observation of a moving target.....- 11 -

Figure 2-1 RADARSAT-1 ScanSAR amplitude image capturing Hurricane Dean on August 17, 2007.....- 24 -

Figure 2-2 RADARSAT-1 ScanSAR amplitude images capturing Hurricane Ivan on September 6, 2004.- 25 -

Figure 2-3 RADARSAT-1 ScanSAR amplitude image capturing Typhoon Xangsane on September 30, 2006.- 26 -

Figure 2-4 RADARSAT-1 ScanSAR amplitude images capturing Hurricane Kyle sequentially on September 26 and 27, 2002.- 27 -

Figure 2-5 RADARSAT-1 ScanSAR amplitude images capturing Hurricane Lili sequentially on September 27, 28, and 30, 2002.- 28 -

Figure 2-6 Flowchart for calculating Doppler velocity from ScanSAR raw data.....- 35 -

Figure 2-7 Procedures for calculating predicted Doppler centroids using the global fitting method and attitude control algorithm (a). Comparison of Estimated and predicted Doppler centroids in range direction before (left) and after (right) applying the attitude control algorithm and improved parameters (b).- 36 -

Figure 2-8 The Doppler velocity during 2001-2007 hurricane season from RADARSAT-1 ScanSAR raw data. Source: Google earth. Red indicates that the sea surface is moving toward the direction of LOS; blue indicates movement away from the satellite.- 50 -

Figure 2-9 Doppler velocities during Hurricane Dean on August 17, 2007. Red indicates that the sea surface is moving toward the direction of LOS; blue indicates movement away from the satellite. - 51 -

Figure 2-10 Doppler velocities during Hurricane Ivan on September 6, 2004. - 52 -

Figure 2-11 Doppler velocities during Typhoon Xangsane on September 30, 2006. - 53 -

Figure 2-12 Track of drifting buoy (September 23, 2006 – October 14, 2006) (a), Velocities of drifting buoy during Typhoon Xangsane (2006) passage (b).- 54 -

-

Figure 2-13 Doppler velocities during Hurricane Kyle on September 26 and 27, 2002, respectively. Here, the color distribution is opposite from sequential Doppler velocities because the left SAR data was acquired in an ascending orbit and the right SAR data was acquired in a descending orbit, respectively. - 55 -

Figure 2-14 Velocity profiles along the azimuth direction for Hurricane Kyle on September 26 (blue line), 2002 and September 27, 2002 (red line). - 56 -

Figure 2-15 Doppler velocities during Tropical storm Lili on September 27, 2002. - 57 -

Figure 2-16 Doppler velocities during Tropical storm Lili on September 28, 2002. Here, the color distribution is opposite from Figure 2-15 and 2-17 because the SAR data were acquired in an ascending orbit. Red colors indicate movement of the sea surface away from the satellite; blue colors indicate movement toward the direction of LOS. - 58 -

Figure 2-17 Doppler velocity during Hurricane Lili on September 30, 2002..- 59 -

Figure 2-18 Grids of 100 × 50 Doppler pixels around the eye of Hurricane Lili on September 27, 2002 (a), September 28, 2002 (b), and September 30, 2002 (c). - 60 -

Figure 2-19 Velocity profiles along the azimuth direction for Hurricane Lili on September 27, 2002 (a), September 28, 2002 (b), and September 30, 2002 (c).

.....	- 61 -
Figure 3-1 Study area (Korea Strait).....	- 67 -
Figure 3-2 Bistatic TanDEM-X ATI interferogram with amplitude as background. - 68 -	
Figure 3-3 Wind speeds at the time of TanDEM-X acquisition (Source: AWS, www.kma.go.kr).	- 70 -
Figure 3-4 Flowchart for calculating a ship velocity using TanDEM-X data from convolutional neural networks	- 72 -
Figure 3-5 (a) TanDEM-X amplitude image detected from wake; (b) edge detection from amplitude image; (c) the linear component from Radon transform; (d) definition of Radon transform on a two-dimensional image; and (e) wake features expressed on the Radon domain.	- 75 -
Figure 3-6 Example of azimuth offset between the detected ship and wake ...	- 77 -
Figure 3-7 Result of ship and wake detection from convolutional neural networks (TanDEM-X data acquired on 2012-02-02, 2012-02-13, 2012-02-24, and 2012-03-06)	- 82 -
Figure 3-8 Result of ship and wake detection from convolutional neural networks (TanDEM-X data acquired on 2012-03-28, 2012-12-06, 2012-12-17, and 2012-12-28)	- 83 -
Figure 3-9 Result of ship and wake detection from convolutional neural networks (TanDEM-X data acquired on 2013-01-08, 2013-01-19, 2013-03-04, and 2013-03-15)	- 84 -
Figure 3-10 Ship velocity from ATI compared to AIS data projected LOS direction	- 88 -
Figure 3-11 TanDEM-X orbit geometry	- 89 -
Figure 3-12 Velocity range response to along-track baseline	- 90 -

Figure A-1 Wind (left) and wave (right) directions under hurricane conditions.
These figures were taken from [Young, 2006]...... - 99 -

Figure B-1 Convolutional Neural Networks for ship and wake detection..... - 103 -

Figure B-2 Example of undetected wake using CNN, wake pattern was relatively
invisible to SAR imaging. - 104 -

List of Tables

Table 2-1 Characteristics of RADARSAT-1 ScanSAR data acquisition	29	-
Table 3-2 Data acquisition of TanDEM-X.....	69	-
Table 3-3 Accuracy of ship velocity from azimuth offset compared to AIS	87	-

1 Introduction

1.1 Overview

SAR (Synthetic Aperture Radar) is one of the most effective tools for velocity measurements. The physical principle to estimate radial velocity utilizes the Doppler shift extracted from SAR data. The Doppler shift is caused by the relative motion between sensor and target. Doppler parameters, such as Doppler centroid frequency and Doppler rate, are the most prominent parameters in SAR processing. The estimation of Doppler parameter can be used as an important source for velocity measurements in various fields including oceanography, geology, civilian, and military. The velocity ranges of the distributed and artificial targets included sea surface current and the moving target velocity was estimated based on the type of SAR products and Doppler parameter estimation techniques as shown in figure 1-1. In this thesis, I examined the distributed target using SAR raw data and the artificial target using SAR SLC data of a single channel SAR system, respectively (Figure 1-2).

First, the Doppler parameter in the received radar signal from SAR raw data is used to retrieve radial Doppler velocity. Doppler velocity is derived by calculating Doppler shift anomalies between the predicted and estimated Doppler centroids. The predicted Doppler centroid is calculated based on a geometric model of satellite by assuming

that the target does not move. The estimated Doppler centroid can be directly extracted from the SAR raw signal data by applying the average cross correlation coefficient method. The characteristics of sea surface velocities in high-wind conditions were investigated by using Doppler centroid measurements from RADARSAT-1 ScanSAR raw data.

Second, the moving target velocity such as ship was investigated by using the azimuth offset between the ship and wake in SAR SLC image. When the SAR SLC data is processed from the raw data, the azimuth compression interprets the Doppler history on the assumption of stationary targets. The relationship between Doppler frequency and azimuth offset is linear, and thus the phase record is identical to that of a similar albeit stationary target located an azimuthal distance away. The azimuth offset between ship and wake is proportional to the Doppler shift effect of the backscattered signal. Thus, the velocity of the ship is estimated by using the azimuth offset between the ship and the wake. I extract the linear component of wake caused by a moving ship. The azimuth offset is precisely estimated by locating the intersection of the linear component to the subpixel position using the edge filter and radon transform. The velocity of the ship was investigated using azimuth offset from TanDEM-X SLC data.

Additionally, we retrieved the ship velocity by using along-track interferometry (ATI) SAR data. The ATI SAR requires two SAR antennas or two SAR systems along the flight direction. The two SAR images were acquired from TanDEM-X (TerraSAR-X add-on for Digital Elevation Measurement) with a short time lag, which

causes the phase difference in the azimuth direction. The along-track interferometry (ATI) phase is proportional to the Doppler shift effect of the backscattered signal and thus related to the radial velocity of the moving target.

Specific applications including distributed target and artificial target velocity can be estimated based on Doppler parameter estimation techniques according to the velocity range. In the next chapter, I describe the theory of a Doppler parameter in the cases of a stationary target and a moving target (Figure 1-2).

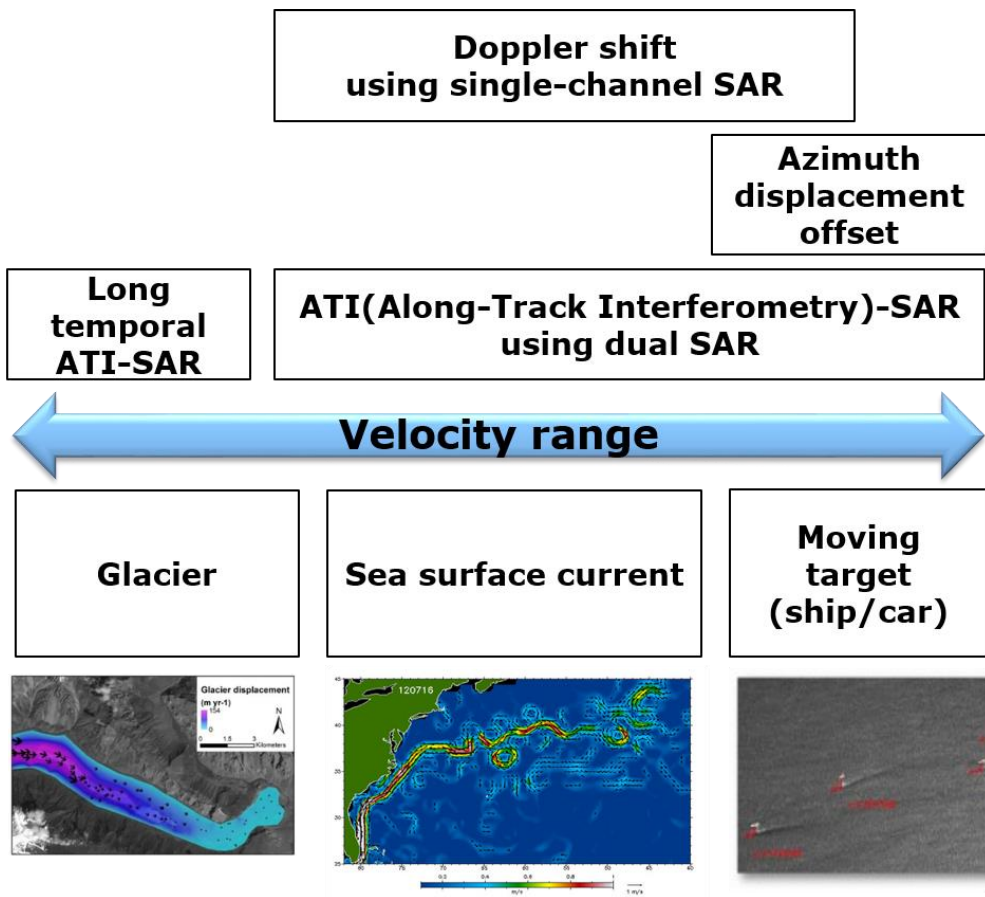


Figure 1-1 Overview of Doppler parameter estimation from SAR for velocity measurements

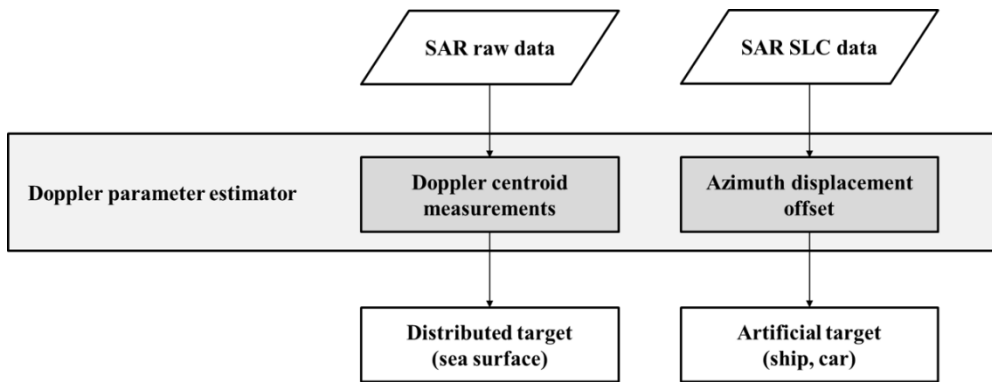


Figure 1-2 Doppler parameter estimator

1.2 Background of Doppler parameter from SAR

An essential part of SAR processing involves the estimation of the Doppler parameters of the received signal. The received SAR signal experiences a Doppler shift due to the relative motion between sensor and target. The average of the Doppler shift is termed as the Doppler centroid frequency. The Doppler centroid frequency is a fundamental parameter for SAR processing. Specifically, the Doppler parameter from SAR is related to the radial velocity of the target on Earth.

The factors that affect Doppler frequency can be described through SAR geometry including satellite orbit, the radar beam pointing direction, and the intersection of the beam with the rotation of the surface of the earth [Cumming and Wong, 2005]. The estimation of Doppler parameters begins with a SAR geometry (Figure 1-3).

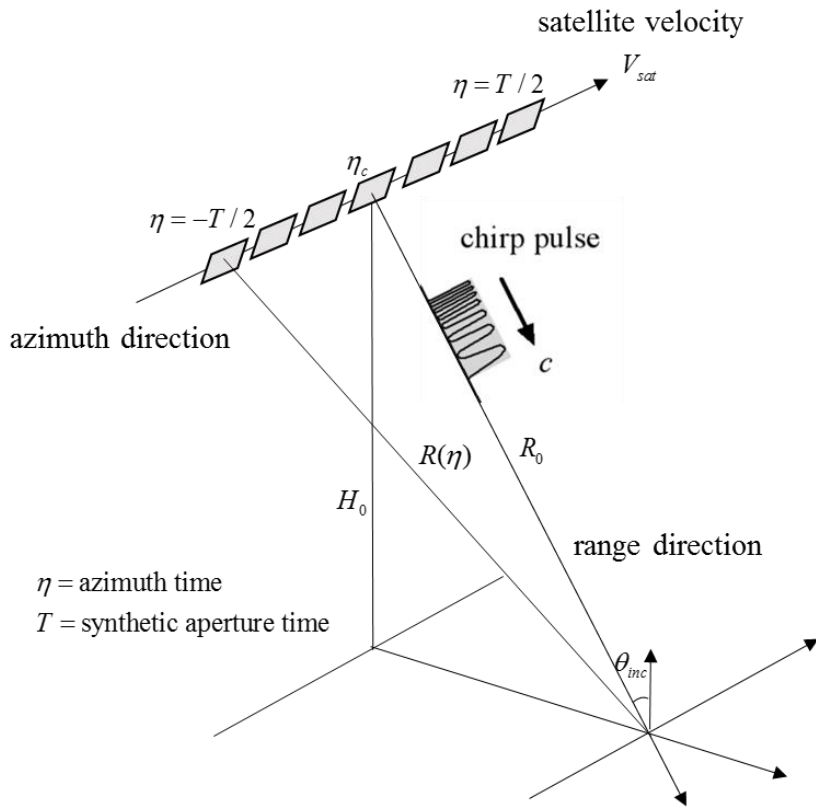


Figure 1-3 SAR geometry

The Doppler effect within 1 pulse is significantly low and is negligible. However, over several subsequent pulses, the Doppler effect is the main factor that shapes the phase of the received signal in the azimuth direction [Li, 2005].

The slant range is a function of azimuth time and is expressed as follows:

$$R(\eta) = \sqrt{R_0^2 + V_{sat}^2 \eta^2} \approx R_0 + \frac{V_{sat}^2}{2R_0} \eta^2 \quad (1-1)$$

where R_0 denotes the slant range, the distance between the Earth's target and the antenna, and V_{sat} denotes the nominal satellite velocity. The approximate expression is obtained by ignoring the high order components of the Taylor expansion.

By using the approximate slant range equation, the azimuth signal is expressed as follows:

$$s_{azimuth}(\eta) = A' \varpi_a(\eta - \eta_a) \exp\left\{-j4\pi \frac{R_0 f_0}{c}\right\} \exp\left\{-j2\pi \frac{V_{sat}^2 f_0}{cR_0} \eta^2\right\} \quad (1-2)$$

The phase of the azimuth signal is expressed as follows:

$$\phi(\eta) = -4\pi \frac{R_0 f_0}{c} - 2\pi \frac{V_{sat}^2 f_0}{c R_0} \eta^2 \quad (1-3)$$

Thus, the Doppler history is expressed as follows:

$$f_a(\eta) = \frac{1}{2\pi} \frac{d\phi(\eta)}{d\eta} = -\frac{2V_{sat}^2 f_0}{c R_0} \eta \quad (1-4)$$

This indicates that the azimuth signal of SAR is also a chirp signal. The chirp signal has two important Doppler parameters. The first parameter corresponds to a Doppler rate and is expressed as follows:

$$K_a = \frac{df_a(\eta)}{d\eta} = -\frac{2V_{sat}^2 f_0}{c R_0} \quad (1-5)$$

Another important parameter is the Doppler centroid that is defined as the Doppler frequency received from a given target on Earth when the target is centered in the

azimuth antenna beam pattern. It represents the azimuth center frequency that is expressed as follows:

$$f_{dc} = f_a(\eta_c) = -\frac{2V_{sat}^2 f_0}{cR_0} \eta_c = \frac{2V_{sat}^2 \eta_c}{\lambda R_0} \quad (1-6)$$

where η_c denotes the beam center crossing time relative to the time of closest approach, and λ denotes the wavelength.

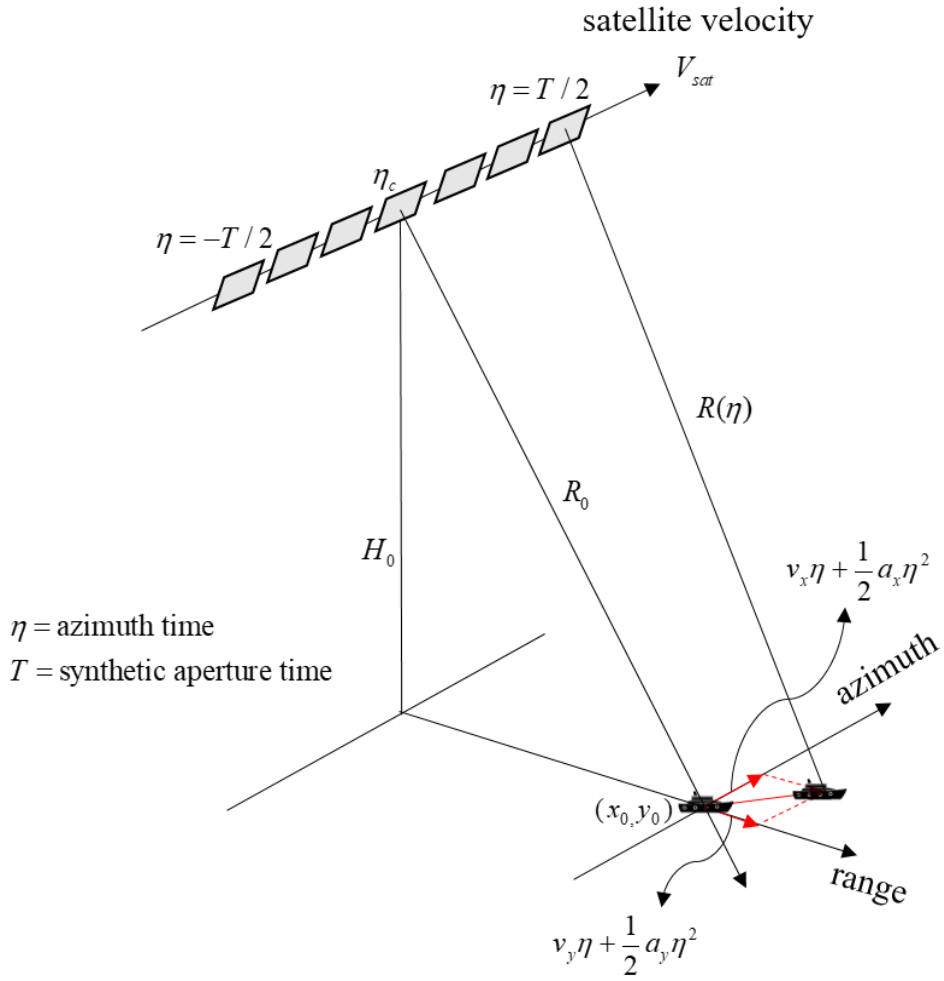


Figure 1-4 SAR geometry in observation of a moving target

However, if moving targets exist in observed SAR scene, then the moving targets are typically azimuthally displaced and defocused in SAR image if their echoes are processed in the same manner as that for stationary echoes [Jao, 2001; Yang and Zhang, 2015]. Thus, I analyze the Doppler parameters on the moving target's azimuth offset in the focused SAR image. With respect to processing SAR imaging, I use the stationary target's Doppler centroid and Doppler rate to process the moving target the azimuth position of moving target in SAR image as follows:

$$\hat{x}_0 = \frac{\lambda R_0}{2V_{sat}} f_{\eta_c} = x_0 \left(1 - \frac{v_x}{V_{sat}}\right) - \frac{y_0 v_y}{V_{sat}} \quad (1-7)$$

At this moment, the azimuth offset of the moving target's imaging distance from its real position is expressed as follows:

$$\Delta \hat{x} = \hat{x}_0 - x_0 = -\frac{x_0 v_x}{V_{sat}} - \frac{y_0 v_y}{V_{sat}} \quad (1-8)$$

Given that SAR processing is in the slant range plane, I use v_r (radial velocity) to denote the projection of v_y in the slant range plane. The relationship between v_r

and v_y are expressed as follows

$$\frac{y_0}{R_0} = \frac{v_r}{v_y} = \frac{a_r}{a_y} = \sin(\theta_{in}) \quad (1-9)$$

For the convenience of the analysis, I assume that $x_0 = 0$ in the following description. Subsequently, the moving target's Doppler centroid is expressed as follows

$$f_{dc_m} = -\frac{2v_r}{\lambda} \quad (1-9)$$

Additionally, its azimuth offset in SAR single look complex (SLC) image is expressed as follows

$$\Delta x = \frac{v_r R_0}{V_{sat}} \quad (1-10)$$

$$\Delta x = \frac{v_g \cos(\theta_{in}) R_0}{V_{sat}} \quad (1-11)$$

where Δx denotes the azimuth offset and θ_{in} denotes the local incidence angle.

The radial velocity of the moving target was obtained in the slant range projection and then converted to ground projection by using local incidence angles.

1.3 Objectives

The thesis focuses on estimating Doppler parameter from SAR (Synthetic Aperture Radar) for velocity measurements. The physical principle for estimating radial velocity utilizes the Doppler shift effect extracted from SAR data. I describe the details of the technique for both Doppler centroid measurements by using SAR raw data and azimuth offset using SAR SLC data, respectively.

The objectives of the thesis, new approaches, and its applications include the following;

- i. The characteristics of the Doppler velocity under high-wind conditions were examined using a considerable number of RADARSAT-1 ScanSAR raw data for a better understanding of the sea surface during hurricanes. Sea surface velocity during tropical cyclones is derived by calculating the Doppler centroid measurements. I used an established model with improved geometric parameters (including slant range distance, look angle, and hour angle), an adjusted ACCC method, and an iterative fitting procedure. The fitting procedure included a global fitting method and an attitude control algorithm for correct biases. I further analyzed the characteristics of the Doppler velocity for various and sequential hurricanes in different oceans and for a single hurricane acquired at

different times.

- ii. The azimuth offset of a moving target such as a ship is proportional to the Doppler shift effect of the back-scattered signal. The ship velocity was derived by calculating the azimuth offset from the TanDEM-X SLC data. To select for the subset data, I automatically detected ships and wakes from SAR images by using the deep-learning-based CNN technique. Under various maritime weather conditions, it is possible to detect the wake by using a manually trained data set with a SAR intensity value. The intersection of a detected wake's linear component is used to identify the accurate reference point of the actual ship's position from Radon transform and edge filtering. Automatic estimation of ship velocity is retrieved by calculating the azimuthal distance with subpixel resolution between the ship and wake. The accuracy of the ship velocity was compared to the ship velocity of the ATI of the TanDEM-X and AIS data, respectively.

2 Retrieval of sea surface velocity during tropical cyclones using RADARSAT-1 ScanSAR Doppler centroid measurements

“Doppler Velocity Characteristics During Tropical Cyclones Observed Using ScanSAR Raw Data [Kang et al., 2016]”

2.1 Background

Tropical cyclones such as typhoons and hurricanes have increased in terms of both strength and frequency over the past 30 years [Emanuel, 2005], causing massive damage and leading to disasters. Such cyclones typically form over warm tropical waters near the equator, where the Coriolis Effect causes air to accelerate towards a central area of low pressure. Due to the increase in strength and extent of tropical cyclones, it is strongly required to observe oceanic responses to tropical cyclones for better understanding of propagation speed, development status, and structure of the cyclones and thus minimize the damages caused by those systems [Katsaros et al., 2002; Reppucci et al., 2010]. The observation and characterization of sea surface currents, waves and winds under extreme conditions have been challenging tasks for many physical oceanographers. It is often difficult to make direct observations under extreme conditions, which also led to a lack of reliable measurements of the initial state of the oceanic response to tropical cyclones and makes poor understanding of the mechanisms of cyclone movement [Friedman and Li, 2000; Alpers and Hennings, 1984; Lyzenga and Bennett, 1988].

Until recently, measurements of sea surface currents have been observed using

various approaches. High-frequency (HF) radar and drifting buoys are the most commonly used in situ tools to measure surface currents. However, HF radar uses a ground-based radar system, which limits the range of data acquisition to coastal areas. Similarly, drifting buoys can only provide point data from their installed locations [Shay et al., 1998; Graber et al., 1996], and there have been inherent difficulties accessing region of interest. Accordingly, it is necessary to develop a new method with capable of observing sea surface currents using suitable satellites even though these data are only available in near real-time or intermittently. Recently, active microwave remote sensing systems such as Quick Scatterometer (QuikSCAT) and Advanced Scatterometer (ASCAT) have been used. Even under extreme conditions, these sensors can penetrate most clouds and make operational measurements at the air–sea interface. However, their spatial resolutions are typically several tens of kilometers [Li et al., 2013]. Oceanic features responding to tropical cyclones can differ from place to place and may be variable even within a small area. In this aspect, space-borne synthetic aperture radar (SAR) can be the most suitable instrument to observe the sea state at high resolution.

In recent times, SAR techniques have been employed to extract sea surface current data over large areas. SAR along-track interferometry (ATI) is one such technique, which uses the phase differences between dual antennas to extract sea surface current data [Kim et al., 2003; Romeiser et al., 2005]. In early 2012, ATI data from TanDEM-X (TerraSAR-X add-on for digital elevation measurement) were obtained from near-optimum baselines. However, such ATI data are currently limited, because the along-

track baselines corresponding to the regions of interest, mostly located in mid- to low-latitude regions, are usually longer than 100 m, resulting in a low temporal coherence [Krieger et al., 2007; Romeiser et al., 2014]. Thus, the applicability of ATI is currently impeded by data availability, despite its success in obtaining high-sensitivity current measurements. To address this, it is also important to use conventional SAR systems to extract present-day sea surface current data.

A previous study using SAR data demonstrates that a Doppler anomaly could be extracted from RADARSAT-1 standard beam raw data and that the Doppler anomaly was directly related to the sea surface currents [Kooij et al., 2001]. In a subsequent study, quantitative sea surface current velocities were estimated from the relationship between surface currents (projected in line-of-sight) and Doppler anomaly using ENVISAT Advanced Synthetic Aperture Radar (ASAR) data [Chapron et al., 2005]. There was a modeling study of sea surface current from RADARSAT-1 standard mode using wavelength diversity ambiguity resolving (WDAR) and multi-look beat frequency (MLBF) algorithm [Marghany, 2009]. Volterra model was also used to simulate the sea surface current from RADARSAT-1 fine mode [Marghany, 2012]. Mostly, the Doppler velocity was dominated by contributions of wind and waves as well as sea surface currents. By subtracting the long wave orbital velocity and phase velocity of Bragg-resonant capillary waves (wind effect) from the total Doppler velocity, the quantitative anomaly should reveal the sea surface current velocity [Moller et al., 1998]. Previous studies focused only on sea surface velocity in low-wind conditions, and an extension of these studies, SAR data have been experimented

to test oceanic responses to tropical cyclones, such as mesoscale circulation responses during the typhoon Man-Yi (2007) [Nam et al., 2012]. Furthermore, wind retrieval from the Doppler shift of wide-swath SAR data has been demonstrated under complex meteorological conditions, such as in atmospheric fronts and low-pressure systems [Mouche et al., 2012]. This study found that the Doppler shift was highly correlated with the wind pattern and hence the method was useful for retrieving more realistic wind directions in case of complex and rapidly changing meteorological situations. However, a quantitative validation of each contribution has not yet been possible for high-wind conditions.

Sea surface current have always been in the center of interest of specialists in different domains of oceanography and marine meteorology. Despite the recent positive results observed based on the Doppler velocity, some issues still need to be addressed. In this study, the characteristics of Doppler velocity in high-wind conditions were examined using a considerable number of RADARSAT-1 ScanSAR raw data for better understanding of hurricanes. In section 2.2, data acquisitions and meteorological history of five different Typhoon and Hurricanes are presented. The methodology of estimating Doppler velocity and its physical interpretation are described in section 2.3. I further analyze the characteristics of Doppler velocity for various Hurricanes in different oceans and for a single Hurricane acquired in different times in section 2.4, and finally made our conclusions in section 4.

2.2 Data set and meteorology

The Western Pacific and the Atlantic Ocean were selected as study area to investigate sea surface velocities under aforesaid extreme conditions associated with tropical cyclones, because these regions are known as the most cyclone-prone regions worldwide. In particular, the Pacific Typhoon Xangsane (2006), the Atlantic Hurricanes Dean (2007), Ivan (2004), Kyle (2002), and Lili (2002) were investigated; Typhoon Xangsane was one of the biggest storms to hit Vietnam in the past several decades, and Hurricane Dean was one of the strongest tropical cyclone of the 2007 Atlantic hurricane season. Similarly, Hurricane Ivan was the 10th most intense Atlantic hurricane ever record, whereas Hurricane Lili was the second deadliest and costliest hurricane of the 2002 Atlantic hurricane season. Hurricane Kyle (2002) was category 1 hurricane that lasted for 22 days and became the 5th longest-lived Atlantic tropical cyclone on record. Thus, these regions were selected as suitable areas for the study of oceanic responses (induced sea surface currents) to extreme tropical cyclones. This study was initially conducted as a part of the RADARSAT Hurricane Applications Project (RHAP) led by the Canadian Space Agency (CSA). RADARSAT-1 ScanSAR data capturing Hurricane Dean, Hurricane Ivan, and Typhoon Xangsane were acquired on August 17, 2007, September 6, 2004, and September 30, 2006, respectively (Figure 2-1, 2-2, and 2-3). In addition, sequential observations of Hurricane Kyle were acquired on September 26 and 27, 2002 (Figure 2-4), and in similar period, Hurricane Lili were also sequentially obtained on September 27, 28 and 30, 2002, respectively (Figure 2-5).

The swath width of RADARSAT-1 ScanSAR mode is approximately between 450-500 km, which is achieved by combining four different beams; wide beams 1 and 2 (W1 and W2) and standard beams 5 and 6 (S5 and S6). As a result, the spatial resolution of the ScanSAR mode is relatively low (about 100 m), but it is high enough to study mesoscale sea surface currents and oceanic responses to hurricanes (Table 2-1). Hurricane-induced changes could be observed in SAR amplitude images. Sea surface imprints of hurricanes such as eye structures, rain bands, and wave patterns around the eye wall were clearly represented in SAR images. For instance, I was able to extract the path of Hurricane Lili, forward speed, the size of its eye, and also its category change from tropical storm to hurricane from figure 2-5. In addition, fine-scale features of the sea surface, which may be difficult to see with other sensors under thick storm clouds, were well observed by the SAR images. The cyclone symbols and corresponding time shown in these figures indicate the position of the hurricane along the moving track of the storm. Typhoon Xangsane was formed on September 25, 2006, in the Western Pacific near the coast of the Philippine Islands. After it grew from a tropical depression to a typhoon, it continued until September 30, 2006, across the China Sea near the coast of the Vietnam. Xangsane maintained its intensity until it approached to Vietnam, where dry air and land interaction began to slowly weaken the typhoon on September 30. Just after 00:00 UTC on October 1, Xangsane was a low-end typhoon, with 10-minute winds of 36 m/s according to the Japanese Meteorological Agency (JMA). On the other hand, Hurricane Dean entered the Caribbean Sea on August 17, and its northern eye wall, accompanied by sustained winds of about 43 m/s, passed directly over Martinique. Subsequently, Hurricane

Dean strengthened to form a Category 4 hurricane and continued to grow steadily in both size and intensity, according to the report of the National Oceanic and Atmospheric Administration (NOAA) National Hurricane Center (NHC) [<http://www.nhc.noaa.gov/>]. Ivan developed from a large tropical wave that moved off the west coast of Africa on 31 August, 2004. Ivan reached its first peak intensity of Category 3, with wind speed of 60m/s at 00:00 UTC on September 6. This made Ivan the southernmost major hurricane on record. Tropical storm Lili acquired a low-level closed circulation on September 27, and its forward speed slowed to about 2.5 m/s by September 28 as it slowly traversed the north coast of Jamaica, traveling northward (Figure 2-4). Then, the storm turned gradually toward the west-northwest while strengthening, eventually becoming a hurricane on September 30. Hurricane Lili reached its peak strength of Category 2 intensity, with wind speed of 34 m/s, on September 30. Kyle (2002) became a hurricane at 12:00 UTC 25 September. A peak intensity of 38m/s is estimated to have occurred at 12:00 UTC 26 September about 683km east-southeast of Bermuda (Figure 2-5). Kyle maintained this intensity for the next 24 hours before gradually weakening under the influence of moderate northwesterly to northerly vertical shear.

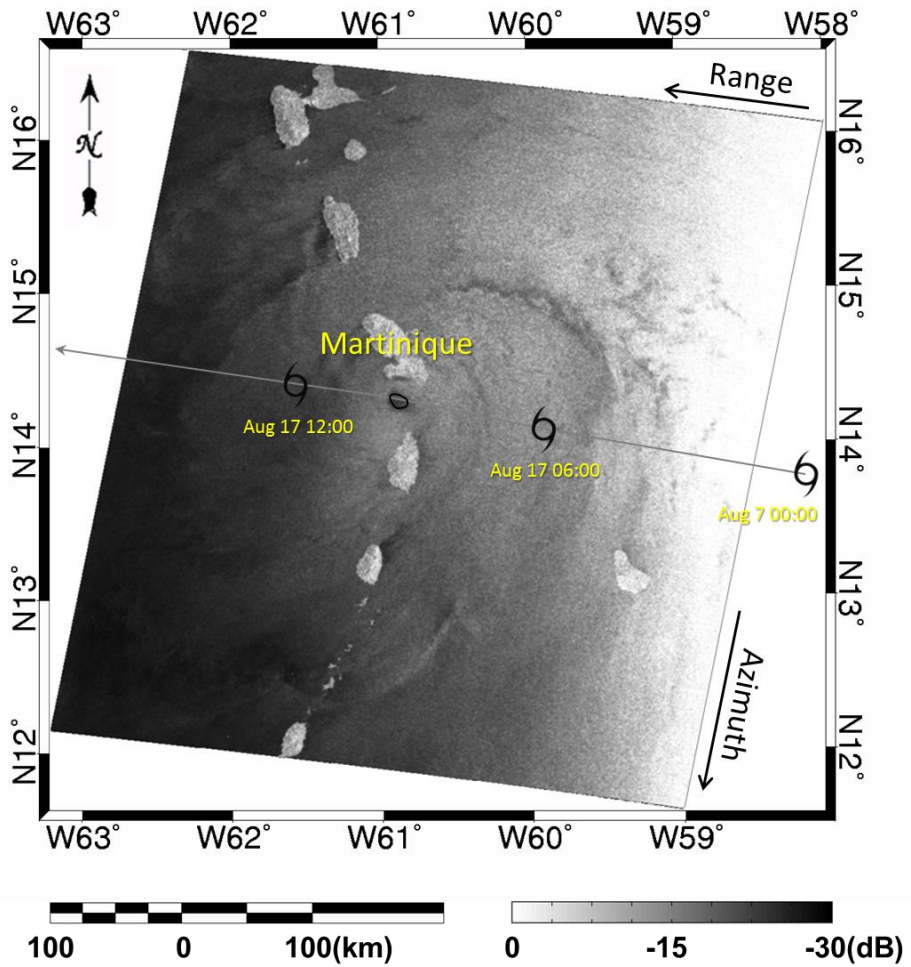


Figure 2-1 RADARSAT-1 ScanSAR amplitude image capturing Hurricane Dean on August 17, 2007.

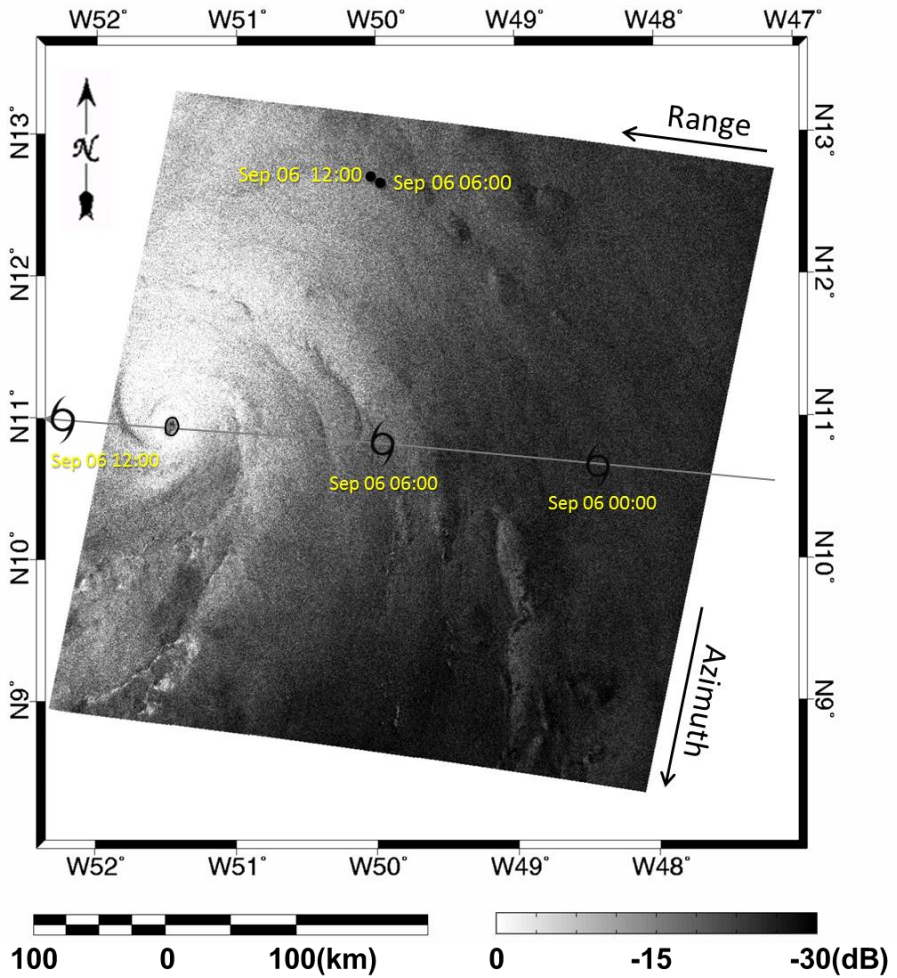


Figure 2-2 RADARSAT-1 ScanSAR amplitude images capturing Hurricane Ivan on September 6, 2004.

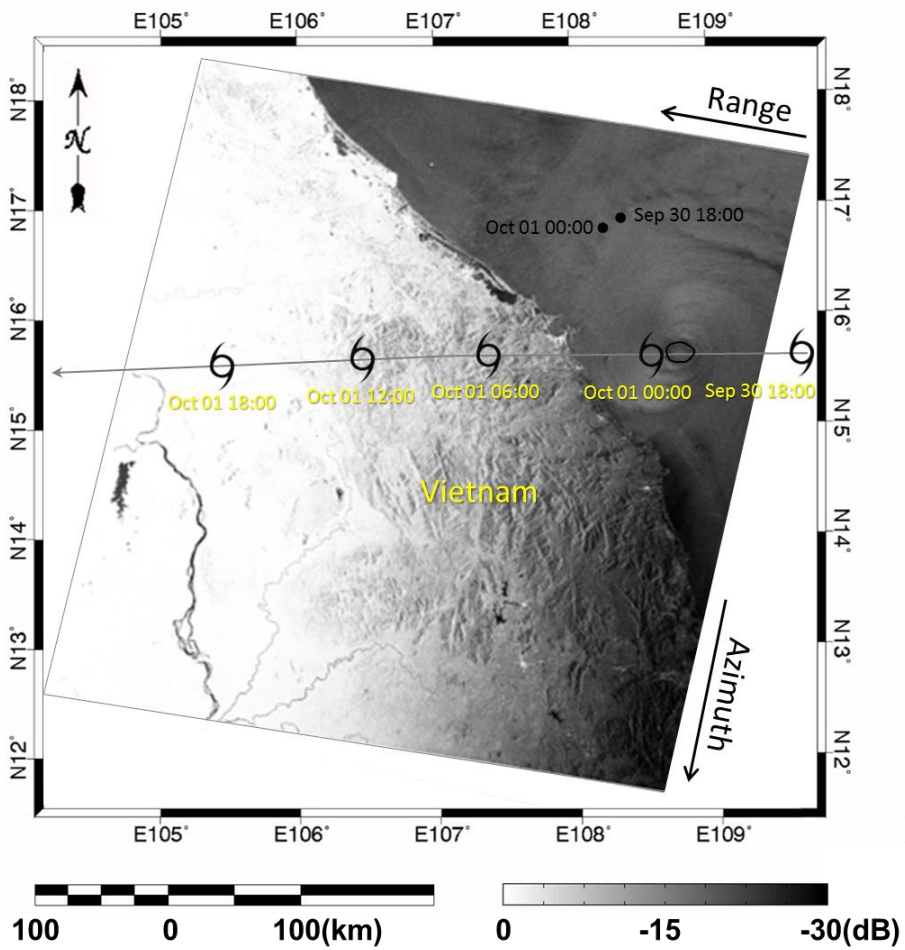


Figure 2-3 RADARSAT-1 ScanSAR amplitude image capturing Typhoon Xangsane on September 30, 2006.

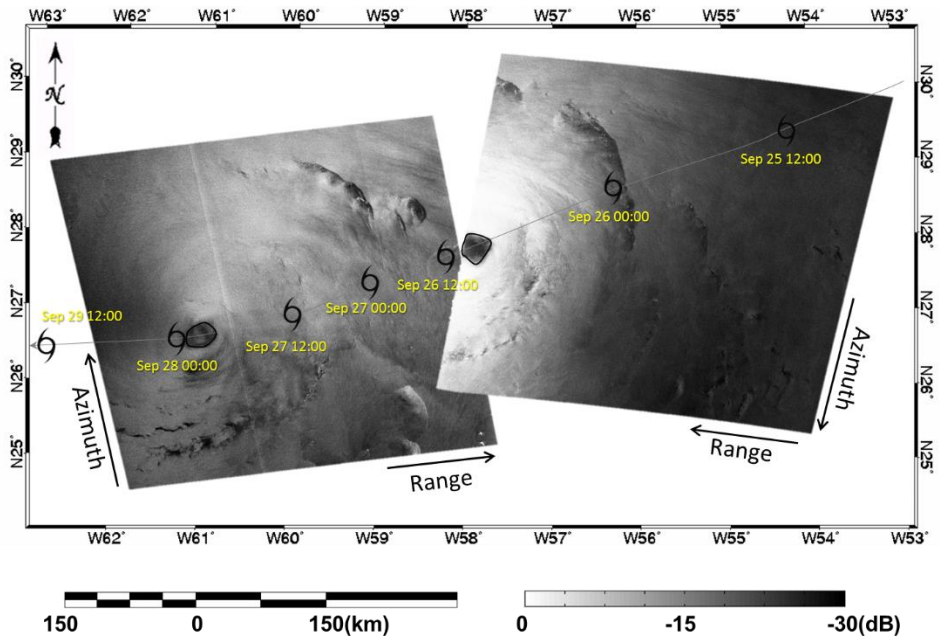


Figure 2-4 RADARSAT-1 ScanSAR amplitude images capturing Hurricane Kyle sequentially on September 26 and 27, 2002.

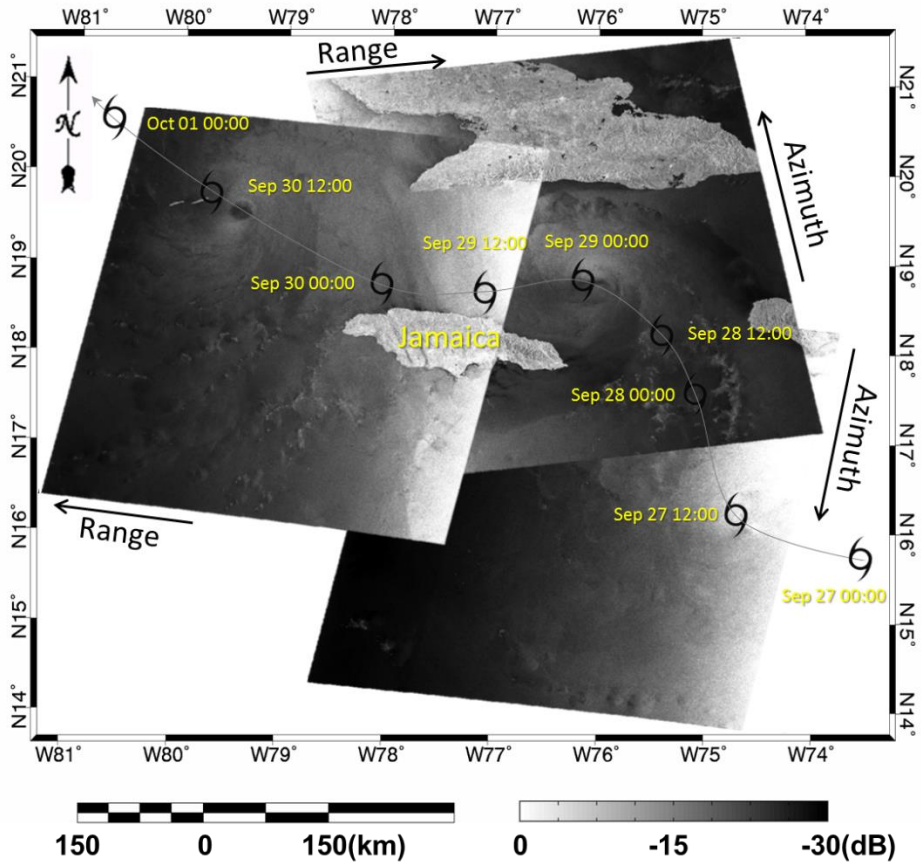


Figure 2-5 RADARSAT-1 ScanSAR amplitude images capturing Hurricane Lili sequentially on September 27, 28, and 30, 2002.

Table 2-1 Characteristics of RADARSAT-1 ScanSAR data acquisition

Name	Hurricane Dean	Hurricane Ivan	Typhoon Xangsane	Tropical storm Kyle	Tropical storm Lili
Location	Atlantic Ocean	Atlantic Ocean	Western Pacific	Atlantic Ocean	Atlantic Ocean
Processing levels	Raw signal data (level 0)	Raw signal data (level 0)			
Acquisition time (UTC)	2007. 08. 17 09:50:26	2004. 09. 06 09:06:53	2006. 09. 30 22:38:32	2002. 09. 26 09:40:20 2002. 09. 27 22:01:52	2002. 09. 27 10:55:00 2002. 09. 28 23:10:59 2002. 09. 30 11:07:02
Orbit type	Descending	Descending	Descending	Descending Ascending	Descending Ascending Descending
Frequency [GHz]	5.3 (C-band)	5.3 (C-band)	5.3 (C-band)	5.3 (C-band)	5.3 (C-band)
Polarization	HH	HH	HH	HH	HH
Beam mode	ScanSAR wide	ScanSAR wide	ScanSAR wide	ScanSAR wide	ScanSAR wide
Spatial resolution [m]	100	100	100	100	100
Incidence angle [°]	19 – 46	19 – 46	19 – 46	19 – 46	19 – 46

2.3 Method

The physical principle for estimating radial velocity utilizes the Doppler shift effect. Doppler shift is caused by the motion of an observer (a SAR sensor) relative to a target (i.e., the sea surface). Sea surface currents can be determined from the Doppler shift anomaly – the difference between the real Doppler shift measured by a moving platform such as the SAR system and the theoretical Doppler shift, which is the Doppler frequency of a stationary (i.e., not moving) surface. Because the SAR platform is always moving, the Doppler frequency corresponding to a specific target is changing as a function of SAR position. The Doppler frequency at the position at which the target is at the beam center is called Doppler centroid. In this thesis, I consider two kinds of Doppler centroids for which the anomalies or residuals infer sea surface motion: the predicted and estimated Doppler centroids.

2.3.1 Predicted Doppler centroid

The predicted Doppler centroid corresponds to a stationary area or fixed target on Earth. It is calculated by considering a SAR imaging platform and the parameters of imaging geometry with respect to the rotating Earth, which include the satellite's orbit, beam pointing direction, and attitude (pitch, roll, and yaw) corresponding to each line

of SAR raw data. In this study, most of the computations were carried out with the following equations given by [Cumming, 2004] and [Cumming and Wong, 2005]. According to their studies, the predicted Doppler centroid is calculated as follows:

$$S_3 = \begin{bmatrix} 1 & 0 & 0 \\ 0 & \cos(\kappa) & -\sin(\kappa) \\ 0 & \sin(\kappa) & \cos(\kappa) \end{bmatrix} \begin{bmatrix} \cos(\gamma) & 0 & -\sin(\gamma) \\ 0 & 1 & 0 \\ \sin(\gamma) & 0 & \cos(\gamma) \end{bmatrix} \begin{bmatrix} R_{sat} \\ 0 \\ 0 \end{bmatrix} \quad (2-1)$$

$$V_3 = \begin{bmatrix} 1 & 0 & 0 \\ 0 & \cos(\kappa) & -\sin(\kappa) \\ 0 & \sin(\kappa) & \cos(\kappa) \end{bmatrix} \begin{bmatrix} \cos(\gamma) & 0 & -\sin(\gamma) \\ 0 & 1 & 0 \\ \sin(\gamma) & 0 & \cos(\gamma) \end{bmatrix} \begin{bmatrix} 0 \\ 0 \\ V_{sat} \end{bmatrix} \quad (2-2)$$

$$U_3 = \begin{bmatrix} 1 & 0 & 0 \\ 0 & \cos(\kappa) & -\sin(\kappa) \\ 0 & \sin(\kappa) & \cos(\kappa) \end{bmatrix} \begin{bmatrix} \cos(\gamma) & 0 & -\sin(\gamma) \\ 0 & 1 & 0 \\ \sin(\gamma) & 0 & \cos(\gamma) \end{bmatrix} \begin{bmatrix} \cos(\psi) & 0 & \sin(\psi) \\ 0 & 1 & 0 \\ -\sin(\psi) & 0 & \cos(\psi) \end{bmatrix} \begin{bmatrix} 1 & 0 & 0 \\ 0 & \cos(\phi) & -\sin(\phi) \\ 0 & \sin(\phi) & \cos(\phi) \end{bmatrix} \begin{bmatrix} -\cos(\alpha) \\ \sin(\alpha) \\ 0 \end{bmatrix} \quad (2-3)$$

where S_3 is the satellite position vector, V_3 is the satellite velocity vector from state vectors, and U_3 is the look vector in Earth-centered inertial (ECI) coordinates. R_{sat} is the altitude of satellite, V_{sat} is the satellite velocity, κ is the inclination angle of orbit, γ is the satellite hour angle from ascending node crossing, ψ is the pitch angle of attitude, ϕ is the yaw angle of attitude and α is look angle between the local vertical and the beam direction. I can obtain the geometry parameters from Leader file of

RADARSAT-1. Particularly, the attitude information, such as pitch and yaw angle, must be considered in rotating coordinates of the look vector.

$$\varphi_g = \theta_{sat_lat_geodetic} - \theta_{sat_lat_geocentric} \quad (2-4)$$

$$U_{3g} = \begin{bmatrix} \cos(\theta_{sat_lon}) & 0 & \sin(\theta_{sat_lon}) \\ 0 & 1 & 0 \\ -\sin(\theta_{sat_lon}) & 0 & \cos(\theta_{sat_lon}) \end{bmatrix}^{-1} \quad (2-5)$$

$$\begin{bmatrix} \cos(\varphi_g) & 0 & -\sin(\varphi_g) \\ 0 & 1 & 0 \\ \sin(\varphi_g) & 0 & \cos(\varphi_g) \end{bmatrix}$$

$$\begin{bmatrix} \cos(\theta_{sat_lon}) & 0 & \sin(\theta_{sat_lon}) \\ 0 & 1 & 0 \\ -\sin(\theta_{sat_lon}) & 0 & \cos(\theta_{sat_lon}) \end{bmatrix} U_3$$

where φ_g is the compensation angle for geodetic latitude, $\theta_{sat_lat_geodetic}$ is the geodetic latitude of satellite, $\theta_{sat_lat_geocentric}$ is the geocentric latitude of satellite, θ_{sat_lon} is the longitude of satellite, and U_{3g} is the look vector considering compensation of between geodetic latitude and geocentric latitude.

$$R_3 = \frac{c}{2} \left(t_{pulse_start} - t_{delay} + \frac{t_{pulse_duration}}{n_{range}} [1 : n_{range}] \right) \quad (2-6)$$

$$P_3 = S_3 + R_3 U_{3g} \quad (2-7)$$

$$Q_3 = \omega_e \sqrt{P_3^2(y) + P_3^2(x)} \begin{bmatrix} -\sin(\theta_{tar_lon}) \\ \cos(\theta_{tar_lon}) \\ 0 \end{bmatrix} \quad (2-8)$$

$$V_{rel} = V_3 \bullet U_{3g} - Q_3 \bullet U_{3g} \quad (2-9)$$

$$F_{pDc} = \frac{2V_{rel}}{\lambda} \quad (2-10)$$

where R_3 is the slant range to target, c is the velocity of light, t_{pulse_start} is the pulse start time, t_{delay} is the pulse delay time, $t_{pulse_duration}$ is the pulse duration time, n_{range} is the number of pixel, P_3 is the target position, Q_3 is the target velocity, ω_e is the Earth's rotation rate, θ_{tar_lon} is the longitude of target, V_{rel} is the relative velocity between satellite and target, and λ is the wavelength. I can obtain beam parameters, such as PRF , the pulse start time, the pulse duration time and attitude information, from auxiliary data of RADARSAT-1 raw data.

Some improvements were carried out in this study for calculating the relative velocity of satellite, such as improving hour angle and look angle when applying the geometric model. The hour angle for each satellite position was calculated in Earth-Centered Inertial (ECI) coordinates. Also, when combined with the temporal information extracted from the line header of the raw data, more accurate positions and velocities for the satellite were derived. Simultaneously, the look angle was recovered from the slant range distances for each beam using parameters from the

auxiliary data. From these data, the sampling rate was calculated by dividing the duration time by the number of pixels in the range direction for each beam. However, time information was required for the transmitted signal to its return; Therefore, it is necessary to compute the actual time of the sensor started to receive the signal. The actual pulse start time was calculated from the duration time and the pulse repetition interval of each beam by comparing the given nominal incidence angles of each beam mode with the arbitrary slant ranges estimated using the Doppler ambiguity numbers. Finally, by subtracting the pulse delay of the starting time of each burst ($4.2 \mu\text{s}$ in the case of the RADARSAT-1 level 0 product), more precise time information and slant ranges were obtained. Calculations of the geometry model were conducted using these improved parameters as inputs. Nevertheless, the altitude of RADARSAT-1 was not accurate enough to determine Doppler centroid within the accuracy of 5 Hz, which corresponds to ~ 0.1 m/s error in velocity for C-band frequency. Thus, an iterative fitting procedure (left part of figure 2-6) was employed to estimate the true altitude of RADARSAT-1 using attitude control algorithm [Marandi, 1998; Eldhuset, 1996] and to fit globally the model for predicted Doppler centroid with the estimated Doppler centroid (global fitting method [Cumming, 2004]). Figure 2-7 shows the result of the predicted Doppler centroid in the range direction after the iterative fitting procedure.

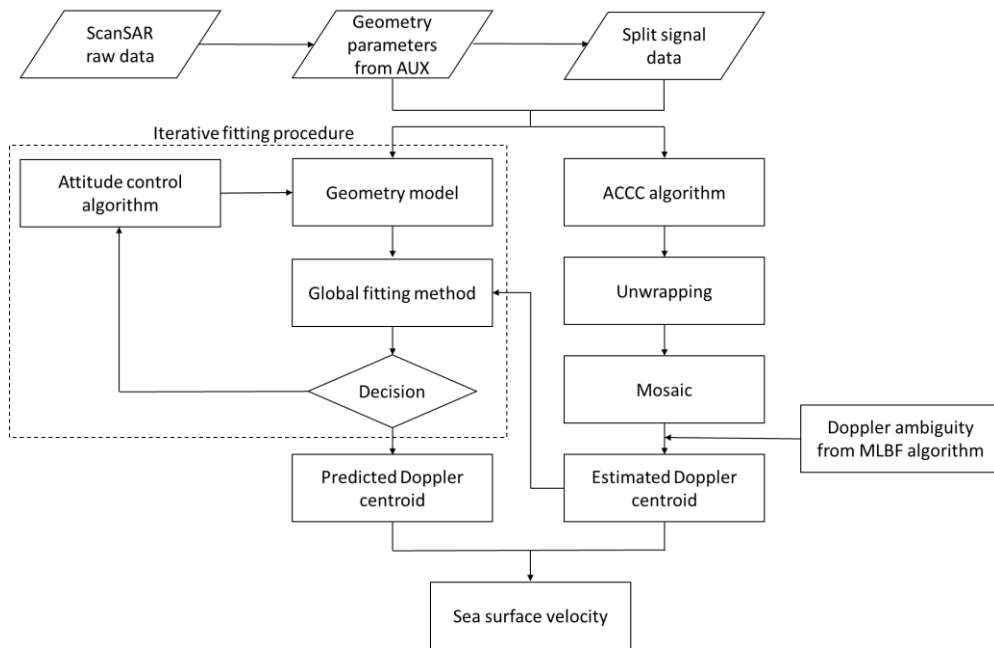
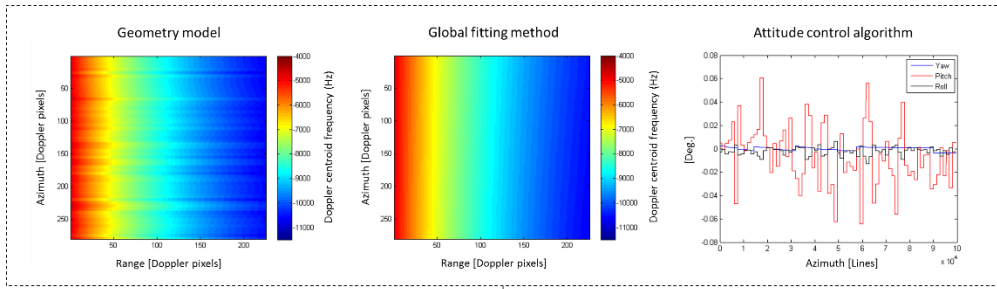
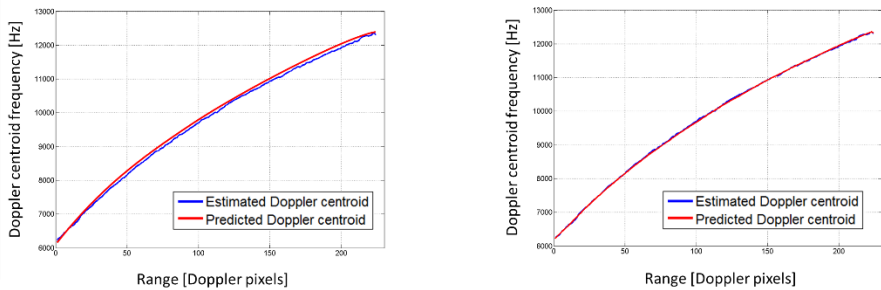


Figure 2-6 Flowchart for calculating Doppler velocity from ScanSAR raw data



(a)



(b)

Figure 2-7 Procedures for calculating predicted Doppler centroids using the global fitting method and attitude control algorithm (a). Comparison of Estimated and predicted Doppler centroids in range direction before (left) and after (right) applying the attitude control algorithm and improved parameters (b).

2.3.2 Estimated Doppler centroid

The estimated Doppler centroid, caused by movement of the upper portion of water column, can be derived by applying the average cross-correlation coefficient (ACCC) algorithm to SAR raw data (right part of figure 2-6). The ACCC algorithm was first proposed by Madsen [Madsen, 1989] and was based on the phase increment from one azimuth sample of the signal to the next. To apply this algorithm, the signal data must be extracted from the SAR raw data. However, the RADARSAT-1 data structure differs from one beam mode to another. For example, the RADARSAT-1 standard mode uses a single beam to record the data during acquisition, and the raw data consists of one data set. However, the RADARSAT-1 ScanSAR mode is separated into four different beams – W1, W2, S5, and S6 – with different parameters for each beam such as pulse repetition frequency (*PRF*), pulse start time, and pulse duration. Furthermore, the beams do not provide continuous coverage; rather, each beam is combined to form a set of bursts. As a result, extraction of correct parameter from the RADARSAT-1 ScanSAR raw data is important for applying the ACCC algorithm to different beams and obtaining continuous Doppler centroids as if the data were acquired with a single beam. The ACCC algorithm can be applied based on the following equations:

$$\overline{C(\eta)} = \sum s^*(\eta)s(\eta + \Delta\eta) \quad (2-11)$$

$$\Phi_{ACCC} = \arg \left[\overline{C(\eta)} \right] = \tan^{-1} \left[\frac{\sum_{\eta} \sin(-2\pi FM_D \eta \Delta \eta)}{\sum_{\eta} \cos(-2\pi FM_D \eta \Delta \eta)} \right] \quad (2-12)$$

where $s(\eta)$ is the azimuth signal, $s^*(\eta)$ is the complex conjugate, and $\Delta \eta$ is $1/PRF$ which is the time increment between two successive azimuth samples. $FM_D = 2V_{sat}^2 f_0 / c R_0$ is the azimuth Doppler FM rate of the signal, f_0 is the center frequency, and R_0 is the slant range. Because η is centered at η_c and the calculation is symmetric, (2-11) can be simplified as:

$$\begin{aligned} \Phi_{ACCC} &= \tan^{-1} \left[\frac{\sin(2\pi FM_D \eta_c \Delta \eta)}{\cos(2\pi FM_D \eta_c \Delta \eta)} \right] \\ &= 2\pi FM_D \eta_c \Delta \eta = -\frac{PRF}{2\pi} FM_D \eta_c \end{aligned} \quad (2-13)$$

According to the relationship between the Doppler centroid and the beam center time, η_c , the estimated Doppler centroid can now be expressed as:

$$F'_{eDc} = -FM_D \eta_c = \frac{PRF}{2\pi} \Phi_{ACCC} \quad (2-14)$$

$$F_{eDc} = F'_{eDc} + M_{amb} PRF \quad (2-15)$$

where, Φ_{ACCC} is the ACCC angle, and M_{amb} is the ambiguity number. It is possible to determine the ACCC angle by using the appropriate patch size. The number of bursts

corresponding to each beam must be suitable for the patch size of ScanSAR mode data. The burst size of RADARSAT-1 ScanSAR is normally 68 lines in the azimuth direction. The calculated ACCC angle is wrapped by 2π in the range direction and it must be unwrapped, particularly for the RADARSAT-1 ScanSAR mode.

Unlike the recently launched satellites like RADARSAT-2 and TerraSAR-X, RADARSAT-1 was not able to operate in yaw steering mode. The yaw steering mode helps to obtain SAR signal data in zero Doppler when the target is located in the center of the beam, which is usually achieved by mechanically or electronically rotating the satellite or its antenna around the satellite's z -axis toward the zero Doppler line [Raney, 1986; Just and Schattler, 1992; Fiedler et al., 2005]. Because of the inability of RADARSAT-1 to operate in yaw steering mode, the amount of Doppler shift may not stay within the baseband of PRF , so that the Doppler ambiguity numbers must be determined to find the absolute Doppler centroid of each beam. To perform this, I applied multi-look beat frequency (MLBF) algorithm presented in [Wong and Cumming, 1996]. The angle unwrapping process was also performed by adding or subtracting 2π to the angle depending on its sign of slope and variance. This unwrapping process removed the modulo- 2π ambiguity and transformed the discontinuous data of the wrapped angles to continuous Doppler angles in the range direction. After calculating the continuous Doppler angles, the data were converted to the Doppler centroid by multiplying by PRF ($M_{amb} \times PRF$), where the Doppler ambiguity number M_{amb} was derived using MLBF algorithm. Finally, the estimated Doppler centroid for each burst was calculated in both range and azimuth directions,

and the average effective spatial resolution was 1×1 km.

2.3.3 Extraction of Sea surface velocity from Doppler shift

The Doppler velocity can be calculated using the difference between the estimated and predicted Doppler centroids, as described above. The locations of the estimated Doppler centroid were exactly matched with the predicted Doppler centroid, based on the acquisition time recorded in each line header of RADARSAT-1 raw data. Then, the Doppler difference was converted to the line-of-sight (LOS) Doppler velocity using the following equation:

$$V_s = \frac{\lambda(F_{eDc} - F_{pDc})}{2 \sin(\theta_l)} \quad (2-16)$$

where V_s is the Doppler velocity projected onto the sea surface, F_{pDc} is the predicted Doppler centroid (Equation 2-10), F_{eDc} is the estimated Doppler centroid (Equation 2-15), λ is the radar wavelength, and θ_l is the local incidence angle [Romeiser and Thompson, 2000]. In this context, the Doppler difference was obtained in slant range projection and then converted to ground projection using local incidence angles.

The correlation between Doppler velocity and sea surface motion has not been

clearly resolved. When Doppler information was first used to estimate sea surface currents, the Doppler velocity was thought to directly represent mean sea surface current velocity [Chapron et al., 2005]. However, later it was found that the Doppler velocity also included contributions from Bragg resonant capillary waves, orbital motion of longer waves, and additional terms induced by long wave motions of the ocean surface [Romeiser et al., 2005; Romeiser and Thompson, 2000]. In recent studies, surface winds and currents were considered as the dominant contributors to the Doppler velocity at moderate sea states [Chapron et al., 2005; Johannessen et al., 2008], while the Doppler shift anomaly showed a strong correlation with wind patterns in high-wind condition [Mouche et al., 2012]. The wind itself cannot introduce a Doppler shift of electromagnetic waves, but instead, the wind-induced surface currents through the drag force and/or Stokes drift due to surface waves can cause the shift of the Doppler frequency. These particle movements are usually amplified in the Doppler velocity resulting from a correlation between locally modulated radar cross sections and facet orbital motions. A detailed description and derivation of this amplification was given in [Chapron et al., 2005] and Appendix A. Because sea surface waves, which cause the Stokes drift, are generated by winds and their amplitudes increase with wind speed, a correlation between Doppler velocity and wind speed seems to be a reasonable assumption. However, the directional characteristics of sea surface waves in hurricane-generated seas can be different from wave characteristics in ordinary wind-generated seas.

Because hurricane-associated wind is a large counter-clockwise (in the Northern Hemisphere) revolving vortex system and the system is advancing in a particular

direction, the initial wind direction at a specific site depends on the direction of movement of the hurricane relative to the site. Additionally, wind direction changes continuously with time. Hence, the directional characteristics of hurricane-generated seas are more complicated [Johannessen et al., 2008]. Several studies [Ochi, 2003; King and Shemdin, 1978; Young, 2006] on the directional characteristics of hurricane-generated seas have shown that the propagation direction of surface waves is not always coincident with the wind direction; rather, surface waves travel in a radial or uni-direction, which are deviated from the local wind directions. Even, it has been observed that wind and wave directions are opposite depending on the location of the hurricane center relative to the site of observation. If the direction of wave propagation is perpendicular to the wind, the velocity bias due to tilt and hydrodynamic modulation of the radar cross section (corresponding to the $\bar{\epsilon}$ of [Chapron et al., 2005]) will be decreased and the Doppler velocity will become close to the sea surface current.

2.4 Result and discussion

The algorithm for estimating Doppler velocity was applied to many RADARSAT-1 ScanSAR raw data acquired during tropical cyclones (Figure 2-8). Among these cyclones, Hurricane Dean (2007), Hurricane Ivan (2004), Hurricane Kyle (2002), Hurricane Lili (2002), and Typhoon Xangsane (2006) were particularly focused to investigate the characteristics of Doppler velocity under hurricane conditions in this study. The ACCC algorithm was applied to all sets of bursts in these ScanSAR data after separation of the raw data into four different beams. After applying unwrapping process, the bursts were mosaicked to form the full swath of the ScanSAR data. Due to inaccurate attitude information of RADARSAT-1, I iteratively applied a global fitting method [Cumming, 2004] for both range and azimuth directions and the attitude control algorithm [Marandi, 1998; Eldhuset, 1996] for calculating Doppler velocity.

The estimated Doppler velocities during Hurricane Dean (2007), Hurricane Ivan (2004), and Typhoon Xangsane (2006) are illustrated in Figure 2-9, 2-10, and 2-11, respectively. The calculations were performed by averaging for an effective spatial resolution of 1×1 km. Land was assumed to be stable and masked with the SAR amplitude image. The black circle represents the radius of the storm's eye. The red color indicates that the sea surface is moving toward the direction of LOS, whereas the blue color indicates the motion away from the satellite. These figures clearly demonstrate that the storms rotate around their eyes in a counterclockwise direction,

which are a typical pattern of tropical storms in the Northern Hemisphere. The velocity patterns show opposite signs in the upper and lower parts of the cyclones and their amplitudes decreased from the center of the cyclones to the outer portions. These patterns show that the Doppler velocity represents the wind-induced drift current including surface Stokes drift. However, it is known that wind-generated surface waves can significantly contribute to the measured Doppler velocity through the correlation between orbital motions of waves and their tilt and hydrodynamic modulation of radar cross section. The comparison with the SAR amplitude image of Figure 2-1 implies that the Doppler velocity extracted from SAR raw data of hurricane has something to do with the (incidence angle corrected) amplitude of the SAR data, which in turn wind speed as assured by [Chapron et al., 2005] and [Mouche et al., 2012]. However, the Doppler velocity in the area where relatively dark features can be seen (believed to be rain bands) is significantly increased (although the direction is reversed), which was not expected in previous studies. Falling rain droplets and dampened surface waves seem to cause the increase in Doppler velocity. Because it was difficult to recognize the propagation direction of surface waves in hurricane-generated seas from RADARSAT-1 ScanSAR data due to their relative low resolution, the amount of 'velocity bias' included in the Doppler velocity was not estimated. However, there were several reports that the longer sea surface waves in hurricane-generated seas propagate in radial or uni-directions, rather than in the wind direction [Ochi, 2003; King and Shemdin, 1978; Young, 2006]. Therefore, the overall Doppler velocity is expected mostly from the hurricane-induced drift current, which is supported by the calculated Doppler velocity of less than 2 m/s. Considering a

velocity bias or amplification of Stoke drift due to the tilt and hydrodynamic modulation of the radar cross section, the Doppler velocity should have been close to ~6 m/s.

The Doppler velocity of Hurricane Ivan was compared to two in-situ drifting buoy data (black dots in Figure 2-10). The two drifting buoy data acquired in 6 hours interval were selected to compare with the closest time of RADARSAT-1 data acquisition. Because the velocities of drifting buoy were given in U (east-west) and V (north-south) components, these velocities were converted into LOS direction. The converted velocities in LOS direction were -0.44 m/s and -0.51 m/s on September 6 06:00 UTC and September 6 12:00 UTC, respectively. Thus, I interpolated two buoy measurements and obtained -0.47 m/s at the SAR acquisition time. On the other hand, the Doppler velocity from RADARSAT-1 raw data was estimated as -0.54 m/s on September 6 09:06 UTC and has difference less than 0.07m/s. Additionally, the Doppler velocity of Typhoon Xangsane was also compared to in-situ current measured by drifting buoy (black dots in Figure 2-11). Two drifting buoy data (every 6 hours) closest to the time of RADARSAT-1 data acquisition showed -1.0 m/s and -0.97 m/s on September 30 18:00 UTC and October 1 00:00 UTC, respectively. The Doppler velocity estimated from RADARSAT-1 raw data showed a quite similar velocity of -1.0 m/s on September 30 22:38 UTC. The velocities of the drifting buoy (-0.97 ~ -1.0 m/s) seemed to be caused by the typhoon-induced drift currents, because the velocities in the LOS direction were relatively slow (-0.6 ~ 0.2 m/s) long before and after Typhoon Xangsane (2006) passages, but the velocities were significantly increased up to -1.0 m/s at the time of SAR data acquisition (Figure 2-11). The

velocity variation of the drift buoy data also supports that the data is reliable and reflects the oceanic responds (induced drift currents) to tropical cyclones.

The sequential observations of Doppler velocities during Hurricane Kyle (2002) on September 26 and 27 are shown in figure 2-13. While comparing right part of Doppler velocities with the left part of Doppler velocities, an inverted color distribution was observed in the left part of Doppler velocities which can be explained by the acquisition of the SAR data in an ascending orbit on September 27. Although two sequential SAR data were acquired in descending (September 26 UTC 09:40) and ascending orbit (September 27 UTC 22:01), the profiles of Doppler velocity around the center of the cyclone's eye show a similar pattern (Figure 2-14). According to NHC report, Hurricane Kyle (2002) maintained the wind velocity of 36 m/s and intensity of category 1 hurricane for more than one day (from September 26 to September 27). At the same time, the profiles of Doppler velocities during Hurricane Kyle (September 26 UTC 09:40 and September 27 UTC 22:01) also showed a consistent pattern regardless of ascending or descending orbit. This pattern indicates that the sea surface currents are mainly affected by the wind blowing above it. This result also indicates that there are no problems with the correction of geometric parameter such as inaccurate orbit and attitude parameter and extraction algorithm. Because the systematic error of RADARSAT-1 ScanSAR was corrected using our method, I could extract the reliable Doppler velocity which was solely induced by the movement of the sea surface. The derived profiles have demonstrated the possibility of applying this technique to characterize the sea surface responses for tropical cyclones.

One particular hurricane (Hurricane Lili (2002)) was captured sequentially by RADARSAT-1 ScanSAR on September 27, 28, and 30, respectively and their Doppler velocities were calculated using our method (Figure 2-15, 2-16, and 2-17). Unlike figure 2-15 or figure 2-17, figure 2-16 exhibits an inverted color distribution which can be explained by the acquisition of the SAR data in an ascending orbit on September 28. Whether ascending and descending orbit data were used, I could observe the opposite sign of Doppler velocities with respect to the cyclone's eye for all data cases (Figure 2-15, 2-16, and 2-17), indicating that the velocities were mostly generated by counterclockwise rotating winds (wind-induced sea surface currents). Additionally, the size of the cyclone's eye on September 30 increased compared to the size of on September 27 while moving toward the west-northwest. To analyze the cyclone development process, I enlarged the Doppler pixels in an area covering 100×50 pixels around the center of the cyclone's eye (Figure 2-18). Generally, the radius of a hurricane eye can be larger as the intensity of a hurricane becomes stronger. The distance between two opposite sign of Doppler velocities around its eye appeared to be increased as tropical storm Lili changed gradually into a Category 2 hurricane. Figure 2-19 shows this change in more detail and it shows Doppler velocity profiles along the azimuth direction around the center of the hurricane's eye. The semi-minor axis of the eye on September 27 was about 4 km when measured as the distance between the maximum and minimum of the Doppler velocities, but it reached 8 km on September 30. During the transition period when Hurricane Lili was passing through the channel between Jamaica and Haiti on September 28, the semi-minor axis decreased to 3 km, which was due to decrease in source of energy (water vapor)

and increased surface friction of the land's terrain. However, an interesting feature was observed during this period. Even though the peak wind speed on September 28 (~23 m/s) was weaker than on September 30 (~34 m/s), the difference between maximum and minimum Doppler velocities around its eye was much higher on September 28 (3.8 m/s) than on September 30 (2.7 m/s), and the overall values were asymmetric between the upper and lower regions of the storm. This seems to have been caused by a fetch-limited sea, surrounded by the landmasses of Jamaica and Cuba. Wind-generated waves in fetch-limited seas can propagate in only one direction. According to the Wave Watch III (WW3) Global Wave Model data, the mean wave direction north of Jamaica was about 115° (in meteorological convention). The correlation between tilt and hydrodynamically modulated radar cross section and the orbital motions of unidirectionally propagating waves can generate additive (in the upper part of a hurricane) or subtractive (in the lower part of a hurricane) Doppler velocities (velocity bias), and thus may have resulted in asymmetric velocities.

In spite of accurate calculations of Doppler centroids, the derived Doppler velocities can have inevitable errors. Low backscattering signals (lower than system noise floor) can generate meaningless Doppler centroids, resulting in abnormal Doppler velocities as shown in the black dashed circle of Figure 2-16. Since the system noise floor (NESZ) of RADARSAT-1 ScanSAR mode is about -26 dB [Manore et al., 2010], I marked the low signal zones where the sigma-naught values were less than -26 dB and disregarded the areas. Another error can be caused by large signal variation in the azimuth direction, in particular where land and ocean meet (land-water boundary). This phenomenon is believed to be one of the errors in estimating Doppler velocity

from RADARSAT-1 raw data.

Although SAR raw data can be used to estimate and thus to understand Doppler velocities under hurricane conditions, more investigations are still required to understand what Doppler velocity represents and how sea surface currents can be estimated from Doppler velocity. According to previous studies [Chapron et al., 2005; Mouche et al., 2012], the Doppler velocity includes not only a quasi-Eulerian current, but also the surface Stokes drift caused by ocean waves and a ‘velocity bias’ caused by the correlation between the locally modulated radar cross section and orbital motions of longer waves. The velocity bias can be small when the directions of surface waves and wind are almost perpendicular. This condition often happens in hurricane-generated seas. Although a validation of estimated surface velocities was difficult to achieve in the present study due to a lack of in situ data, our results illustrate a typical sea surface response to tropical cyclones. These results are encouraging, and should open up new avenues of scientific research.

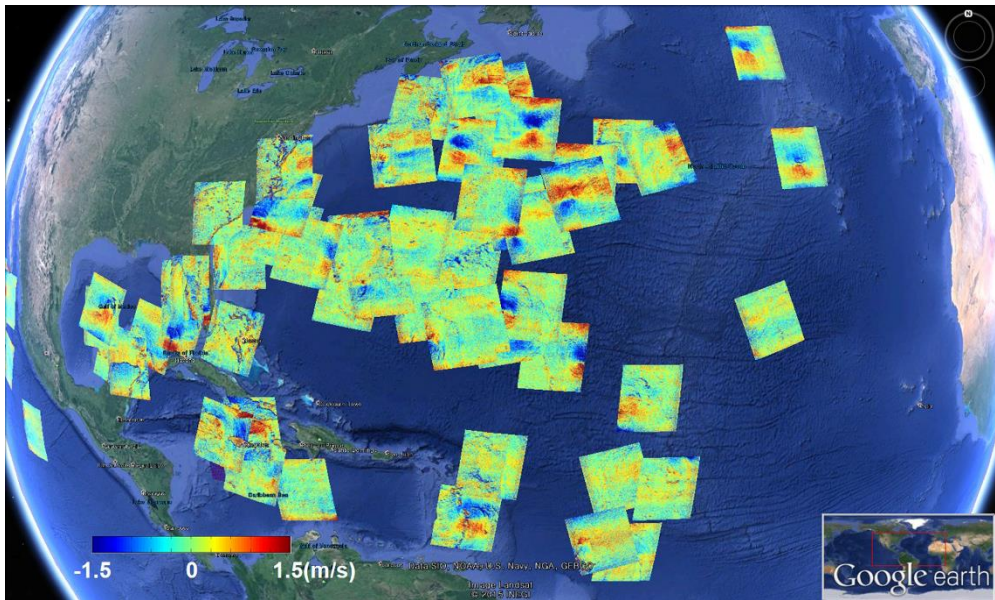


Figure 2-8 The Doppler velocity during 2001-2007 hurricane season from RADARSAT-1 ScanSAR raw data. Source: Google earth. Red indicates that the sea surface is moving toward the direction of LOS; blue indicates movement away from the satellite.

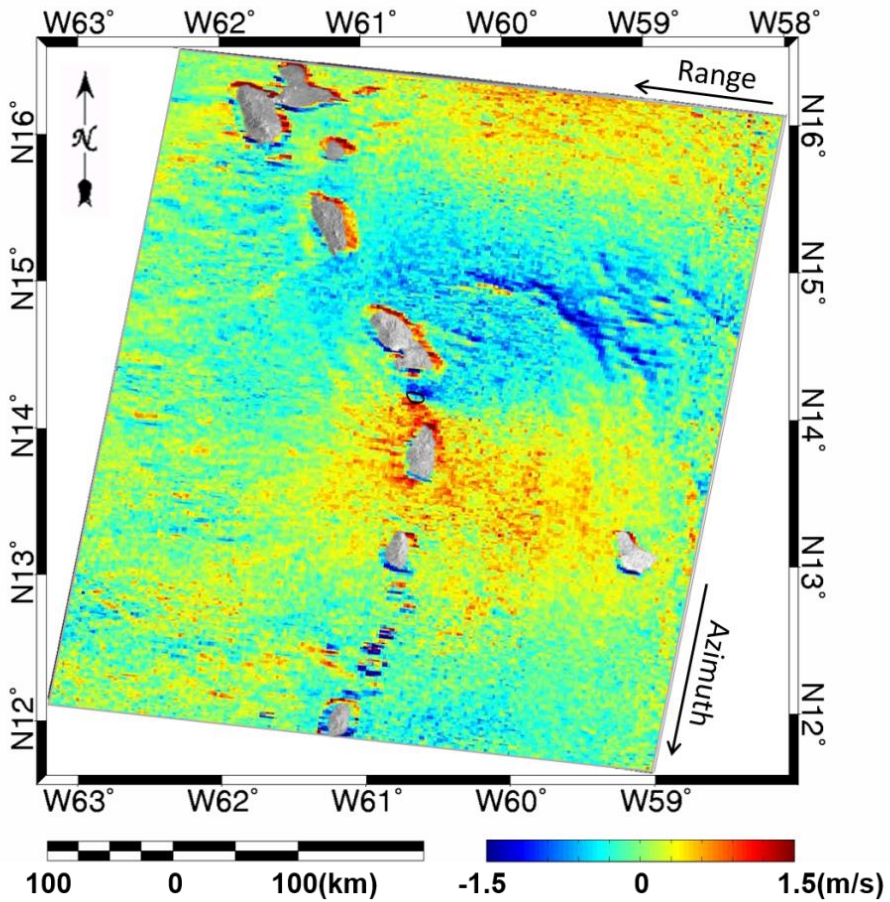


Figure 2-9 Doppler velocities during Hurricane Dean on August 17, 2007. Red indicates that the sea surface is moving toward the direction of LOS; blue indicates movement away from the satellite.

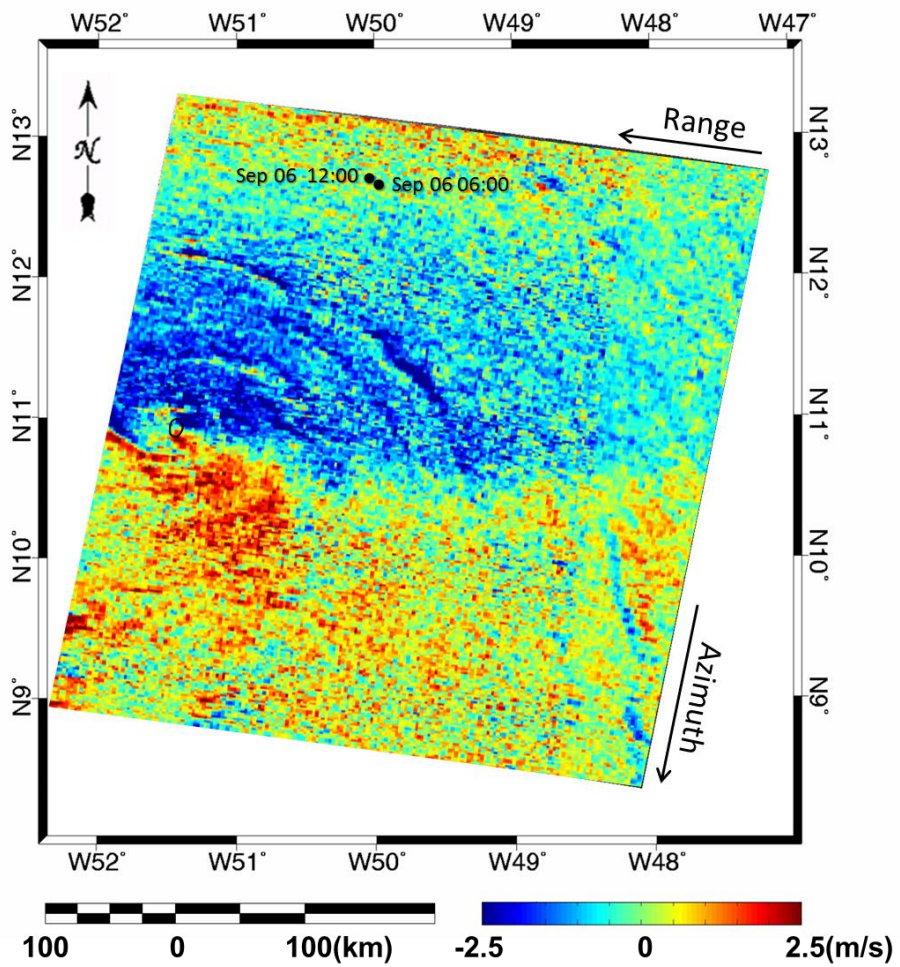


Figure 2-10 Doppler velocities during Hurricane Ivan on September 6, 2004.

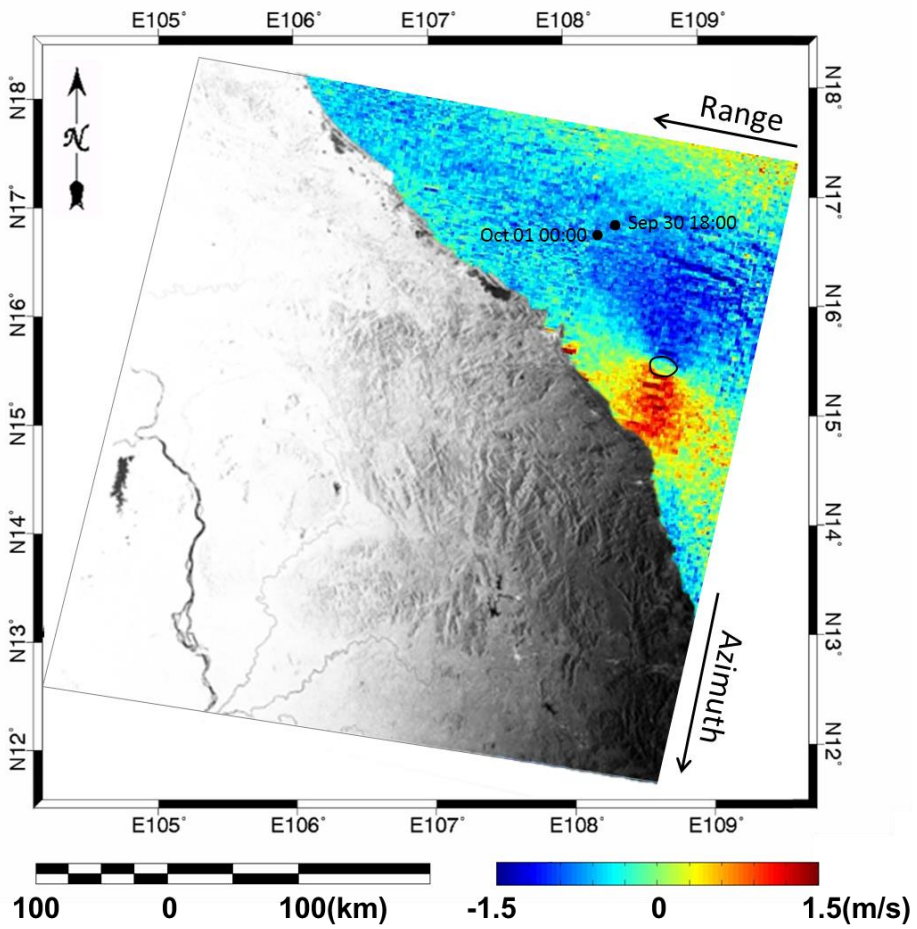
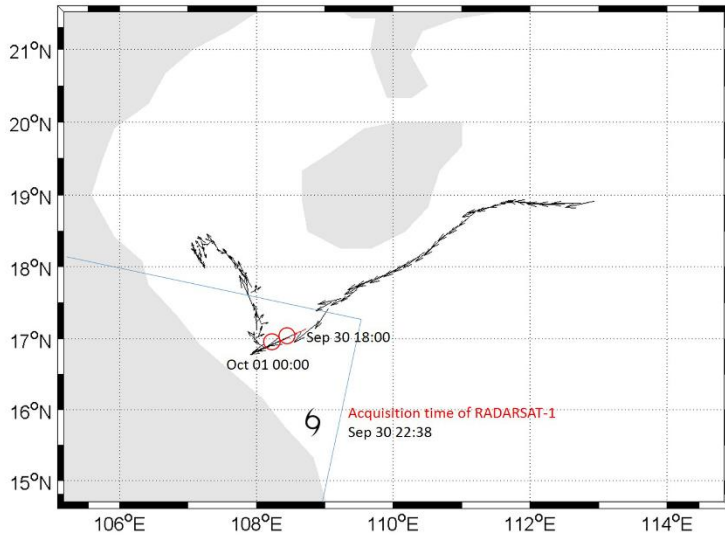
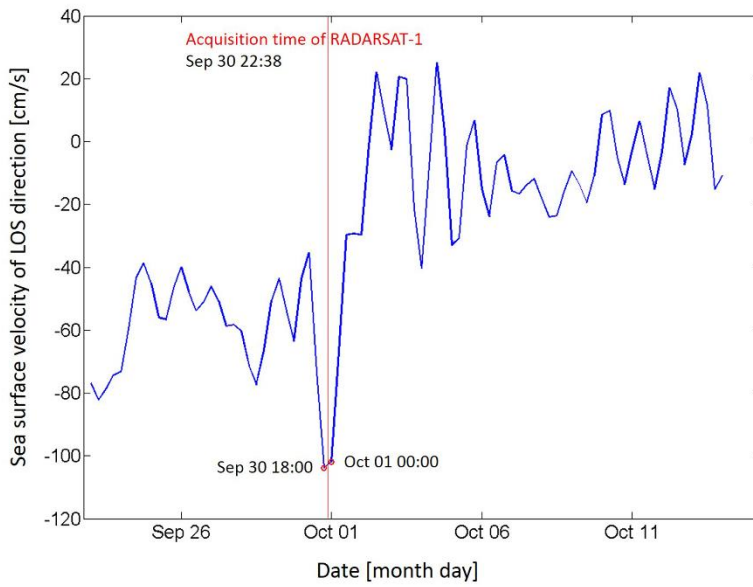


Figure 2-11 Doppler velocities during Typhoon Xangsane on September 30, 2006.



(a)



(b)

Figure 2-12 Track of drifting buoy (September 23, 2006 – October 14, 2006) (a), Velocities of drifting buoy during Typhoon Xangsane (2006) passage (b).

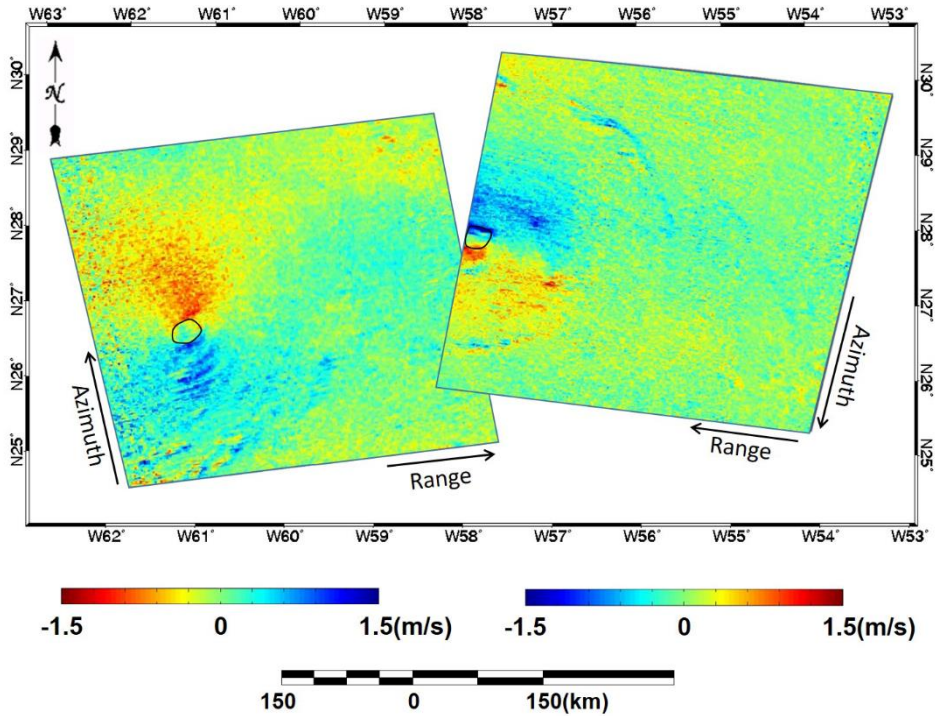


Figure 2-13 Doppler velocities during Hurricane Kyle on September 26 and 27, 2002, respectively. Here, the color distribution is opposite from sequential Doppler velocities because the left SAR data was acquired in an ascending orbit and the right SAR data was acquired in a descending orbit, respectively.

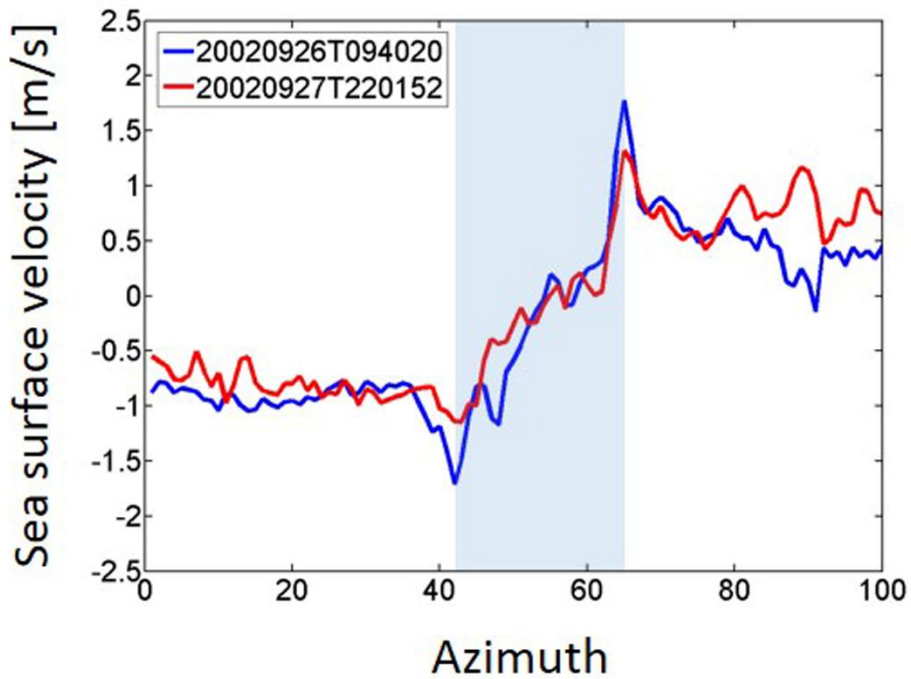


Figure 2-14 Velocity profiles along the azimuth direction for Hurricane Kyle on September 26 (blue line), 2002 and September 27, 2002 (red line).

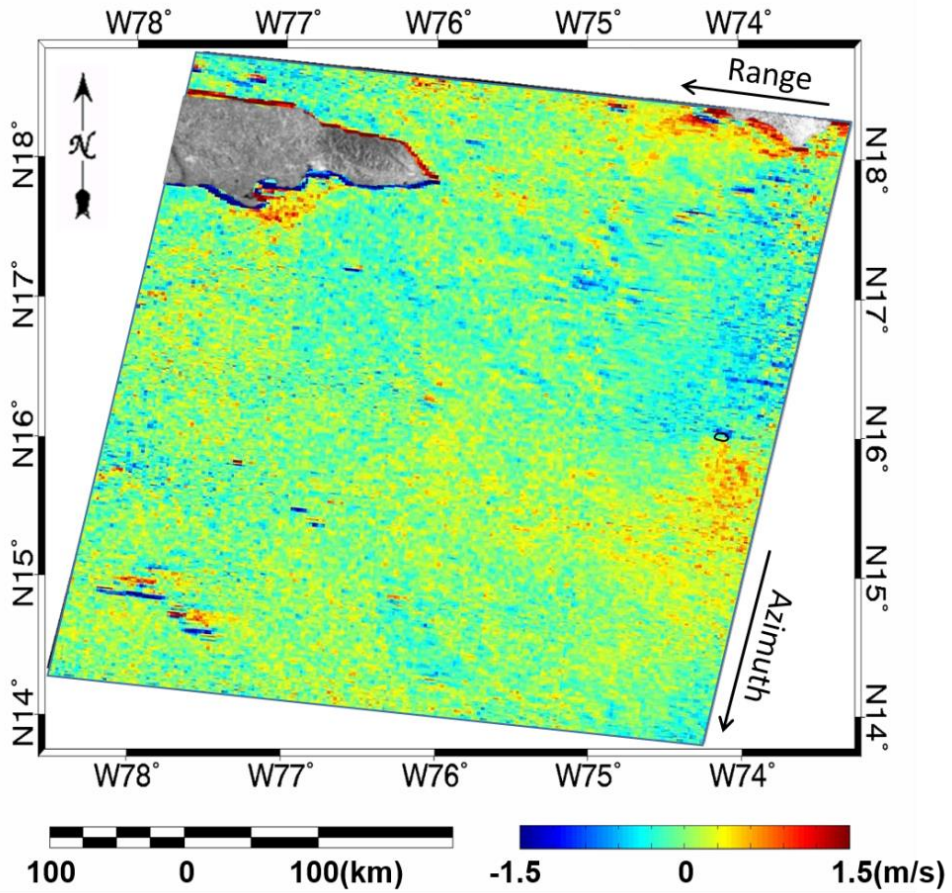


Figure 2-15 Doppler velocities during Tropical storm Lili on September 27, 2002.

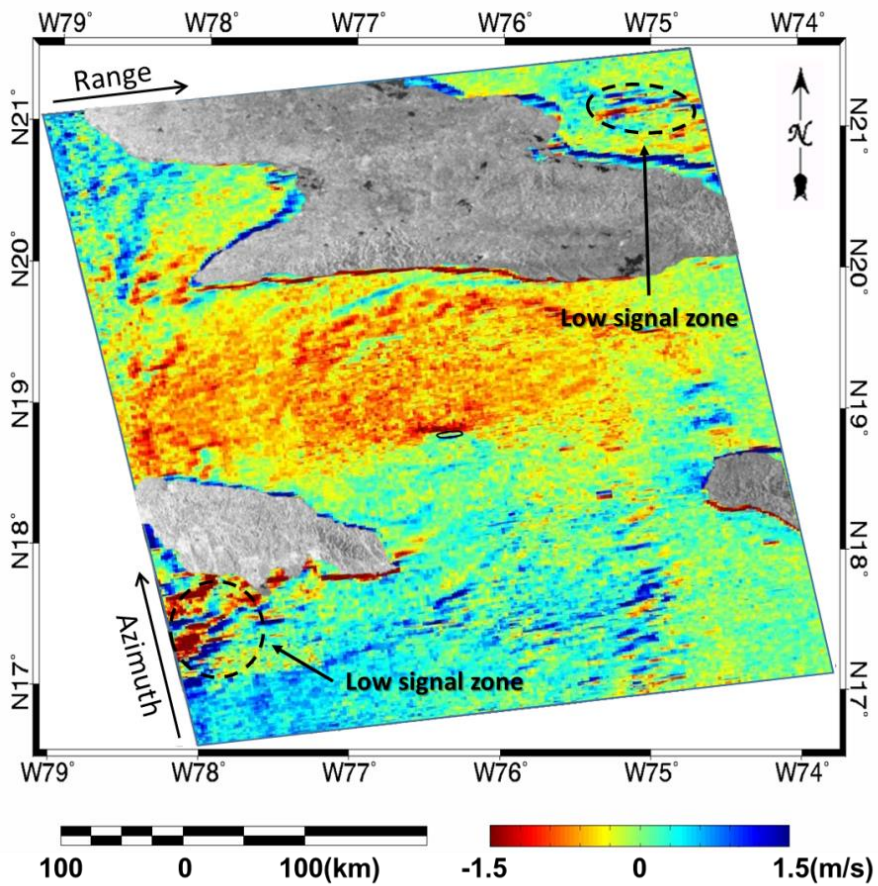


Figure 2-16 Doppler velocities during Tropical storm Lili on September 28, 2002. Here, the color distribution is opposite from Figure 2-15 and 2-17 because the SAR data were acquired in an ascending orbit. Red colors indicate movement of the sea surface away from the satellite; blue colors indicate movement toward the direction of LOS.

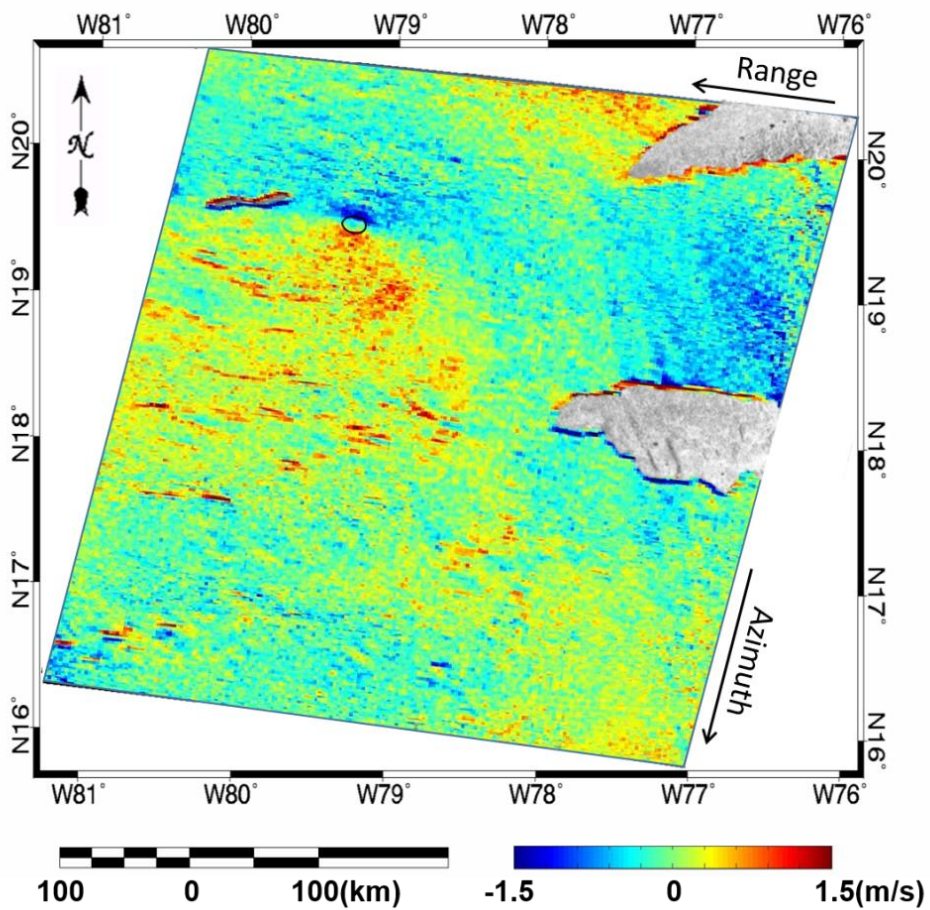


Figure 2-17 Doppler velocity during Hurricane Lili on September 30, 2002.

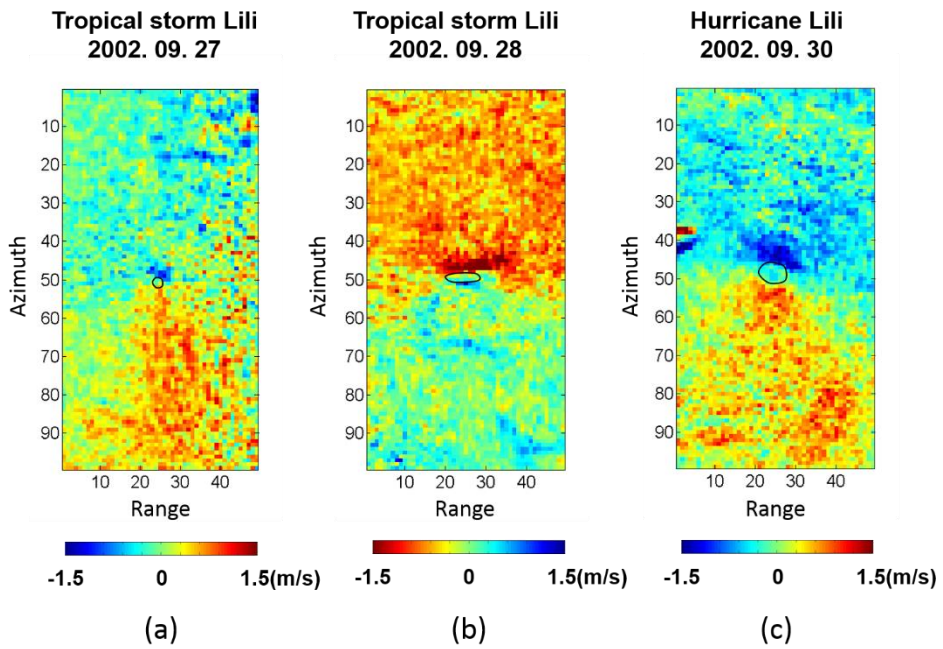


Figure 2-18 Grids of 100×50 Doppler pixels around the eye of Hurricane Lili on September 27, 2002 (a), September 28, 2002 (b), and September 30, 2002 (c).

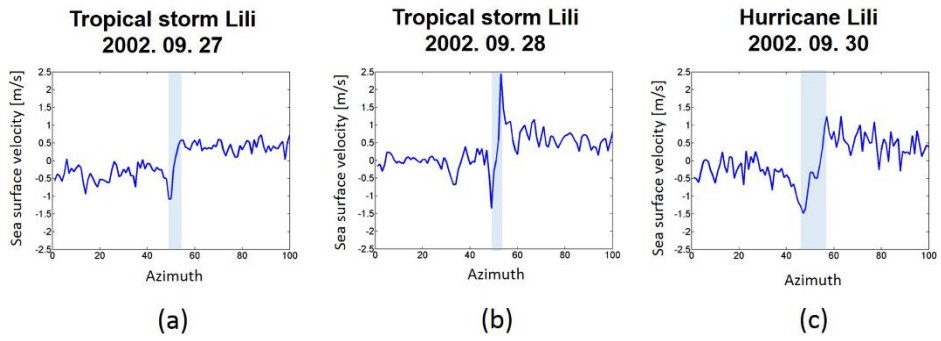


Figure 2-19 Velocity profiles along the azimuth direction for Hurricane Lili on September 27, 2002 (a), September 28, 2002 (b), and September 30, 2002 (c).

3 Retrieval of ship velocity using azimuth offset from TanDEM-X SLC data

3.1 Background

Surveillance of maritime traffic is an important security topic in certain parts of the world and even more in recent years. Recently, automatic identification systems (AISs) were installed in every active ship, and maritime traffic information is monitored in real time by using these systems. However, AIS occasionally loses functionality in the event of maritime accidents, and it is not possible to track the location of drifting ships. Illegal pair trawling by unpermitted ships without AIS is another significant issue that requires a solution. Therefore, research to spatially monitor numerous ships in the ocean is of vital importance.

Ship monitoring included location and velocity information can prevent maritime accidents. Various algorithms that are based on Synthetic Aperture Radar (SAR) imagery are currently under development for spatial ship detection and velocity estimation. Research in ship detection includes moving target indicator algorithms (MTI) that detect a moving object and wake detection algorithms that detect the wake created by a moving ship. Previous studies on ship detection on the sea surface involved RADARSAT-1 images through a statistical approach using wind speed, incidence angle, and resolution [Vachon et al., 1997]. Ships and wakes were detected using the thresholds of different intensity values of SeaSat and ERS-1 satellite images,

respectively [Eldhuset 1996]. Ship wakes appear in SAR images as dark or bright straight lines, and existing algorithms for wake detection exploit the linear component detection algorithms such as Radon transforms [Graziano et al., 2016]. Several studies have developed wake detection techniques for SAR images by using Radon transform [Rey et al., 1990; Copeland et al., 1995; Scherbakov et al., 1996; Zilman et al., 2004]. However, these studies only focused on a few case studies using manually selected subset data from the SAR images.

Recent studies have used several training set data to detect ships by using deep learning techniques such as convolutional neural networks (CNN) for image-based feature extraction [Schwegmann et al., 2016; Zhang et al., 2016; Liu et al., 2017]. Deep learning techniques calculate weighting factors by using training set data on varying recording environments and maritime weather conditions, thereby increasing the probability of ship detection. However, most studies that use deep learning techniques focus on methods to detect target objects instead of wake components. This is because a moving ship creates strong back scattering that is independent from the sea clutter, and motionless and slowly moving ships do not create wakes. There is a paucity of studies using MTI that use deep learning to detect both ships and wakes.

Several studies estimated ship velocity and beam by using the wake created by a moving ship observed in SAR images [Graziano et al., 2014; Graziano et al., 2016; Graziano et al., 2017; Kang et al., 2017]. An algorithm of ship wake detection requires a relatively more complex process of calculation and greater processing time. A disadvantage of this approach is that wakes are not clearly visible in images acquired

at high incidence angles. It is difficult to estimate ship velocity with high accuracy based on a limited range of information such as wake patterns, directions, and sizes. Under various maritime weather conditions, it is possible to detect the wake by using deep learning based on CNN with manually trained data sets. By using the wake component from deep learning, the ship velocity can be estimated detected from a single SAR image because of the azimuth offset between the ship and wake. Two bright or dark linear components are the signature of a turbulent wake, which are aligned with the ship longitudinal axis.

Furthermore, a method to determine the radial velocity of moving target employs the phases of a multi-channel along-track interferometric SAR system [Kim et al., 2003; Budillon et al., 2008;]. Recent dual SAR systems such as TerraSAR-X and TanDEM-X are suitable to estimate relatively slow-moving targets, such as sea surface currents or ships velocity, due to longer baselines in the along-track direction. However, the ATI phase only yields that of the phase wrapped in 2π . Relative velocity using wrapped phase is required to resolve the ambiguity velocity for absolute velocity. The most effective method to calculate absolute velocity from a single SAR image involves using azimuth offset from a ship to the wake. When the SAR SLC image is processed from the raw data, the azimuth compression interprets the phase history based on the assumption of stationary targets. The relationship between Doppler frequency and azimuth offset is linear, and thus the phase record is identical to that of a similar albeit stationary target located an azimuthal distance away. Thus, it can resolve the ambiguity velocity of the ship that is estimated by using accurate

azimuthal distance between a ship and the wake.

In this study, I automatically detected ships and wakes from SAR images by using deep learning based on the CNN technique. By automatically selecting the wake's subset data, the linear component of the wake was used to identify the accurate reference point between the ships and wakes from Radon transform and edge filtering. The objective of this study involved estimating the ship velocity by calculating the azimuth offset of the subpixel between the ship and wake. The accuracy of the ship and wake detection rate was compared to AIS data. Furthermore, the accuracy of the estimated ship velocity was validated by using the ship velocities from the ATI and AIS data.

3.2 Study area and data acquisition

The Korea Strait was selected as the study area to estimate ship velocity by using TanDEM-X SLC images (Figure 3-1). The Korea Strait are bounded by the southern coast of the Korean peninsula and the southwestern coast of Japan. A branch of the Kuroshio Current also passes through the strait. In this region, surveillance of maritime traffic is an extremely important security topic.

A total of 12 scenes from TanDEM-X data dating from 2012/02/02 to 2013/03/15 were used for estimation (Figure 3-2). Table 3-1 shows the weather conditions at the recorded time including wind direction and wind speed. All data used were in descending mode, and the incidence angle was approximately 21° . The averaged coherence in most of the images is below 0.4. Thus, I analyzed both along-track and across-track baselines for all pairs. As shown in Figure 3-3, the wind speeds at the time of TanDEM-X acquisition were relatively low with small variations ranging from 1.4 to 5.5 m/s except on December 17, 2012 (7.9 m/s).

The baselines of TanDEM-X vary based on latitude due to helix orbit formation. Generally, a decrease in the along-track baseline improves the conditions to obtain the ATI phase required to determine moving target velocity. In order to test the accuracy of the ship velocity determination, the data were converted to the LOS direction using ship direction and velocity from the AIS data over the same time period acquired by TanDEM-X.

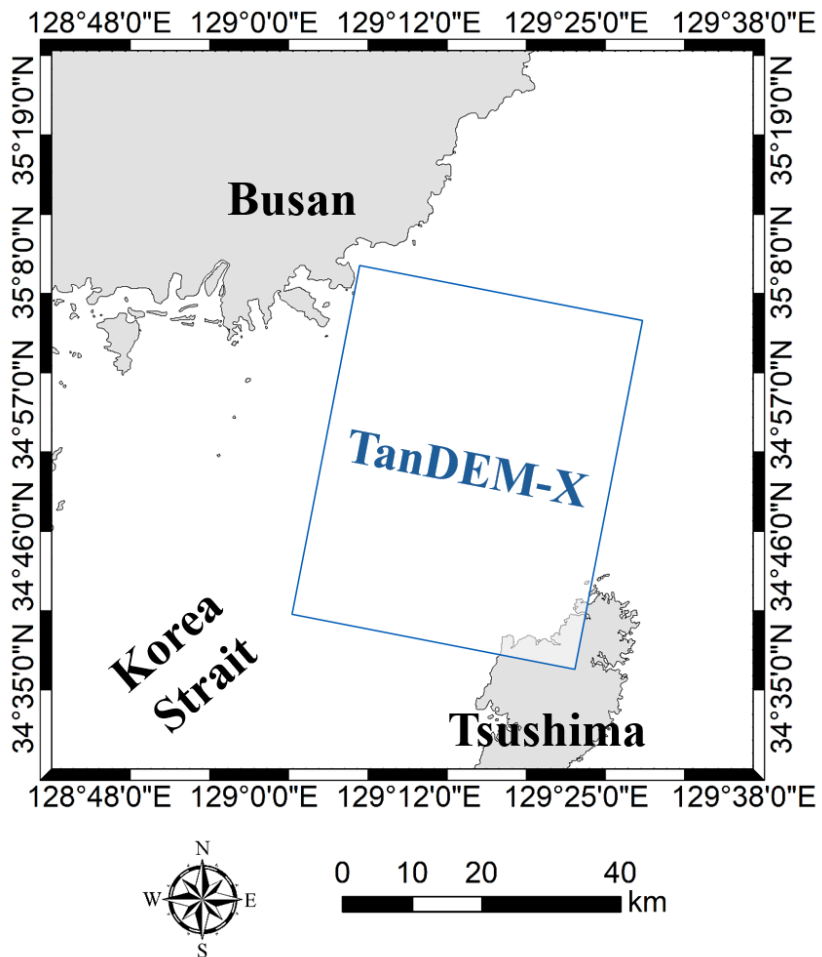


Figure 3-1 Study area (Korea Strait)

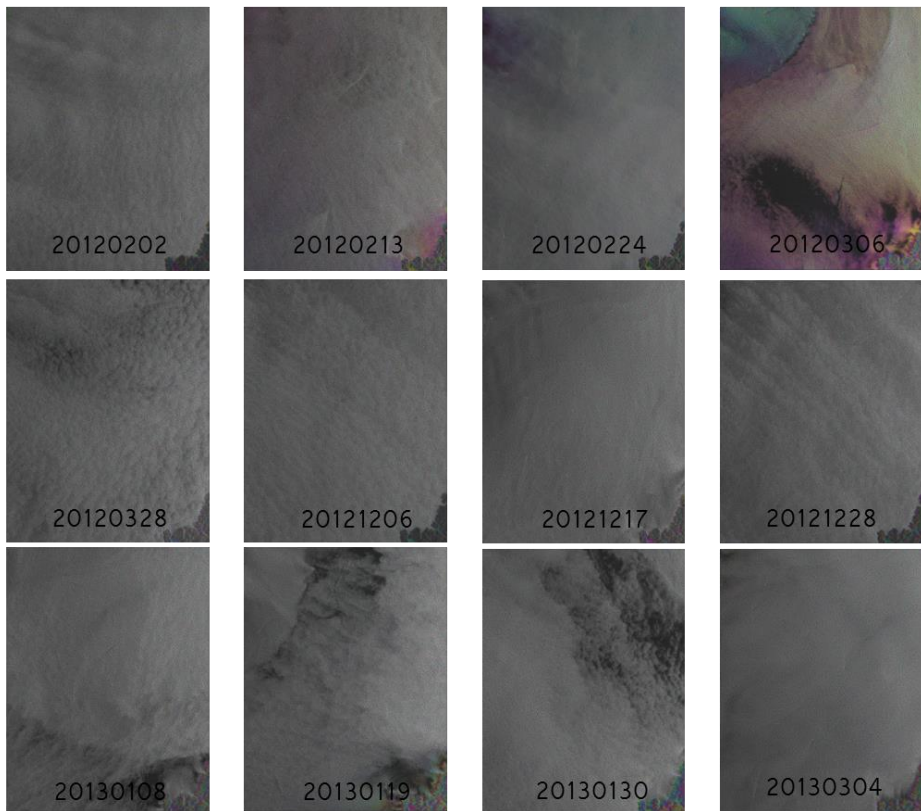


Figure 3-2 Bistatic TanDEM-X ATI interferogram with amplitude as background.

Table 3-2 Data acquisition of TanDEM-X

Time UTC	Mode	Orbit	Average coherence	ATI baseline [m]	Incidence angle [°]	Velocity range [m/s]	Wind direction [°]	Wind speed [m/s]
2012-02-02T21:35:47	Bistatic	Descending	0.38	141.73	21.52	2.30	337.5	2.8
2012-02-13T21:35:46	Bistatic	Descending	0.37	128.38	21.53	2.55	22.5	2.6
2012-02-24T21:35:46	Bistatic	Descending	0.43	127.95	21.51	2.56	22.5	5.5
2012-03-06T21:35:46	Bistatic	Descending	0.39	128.05	21.51	2.56	270	1.8
2012-03-28T21:35:47	Bistatic	Descending	0.39	124.70	21.53	2.62	22.5	1.6
2012-12-06T21:35:53	Bistatic	Descending	0.34	349.17	21.50	0.94	270	1.4
2012-12-17T21:35:52	Bistatic	Descending	0.34	309.39	21.50	1.06	270	7.9
2012-12-28T21:35:52	Bistatic	Descending	0.34	337.02	21.50	0.97	337.5	1.9
2013-01-08T21:35:52	Bistatic	Descending	0.34	335.58	21.50	0.98	270	5.1
2013-01-19T21:35:51	Bistatic	Descending	0.34	305.84	21.52	1.07	337.5	2.9
2013-01-30T21:35:51	Bistatic	Descending	0.34	311.31	21.51	1.05	315	1.7
2013-03-04T21:35:51	Bistatic	Descending	0.35	273.37	21.50	1.20	270	3.2
2013-03-15T21:35:52	Bistatic	Descending	0.35	219.62	21.50	1.49	247.5	3.0

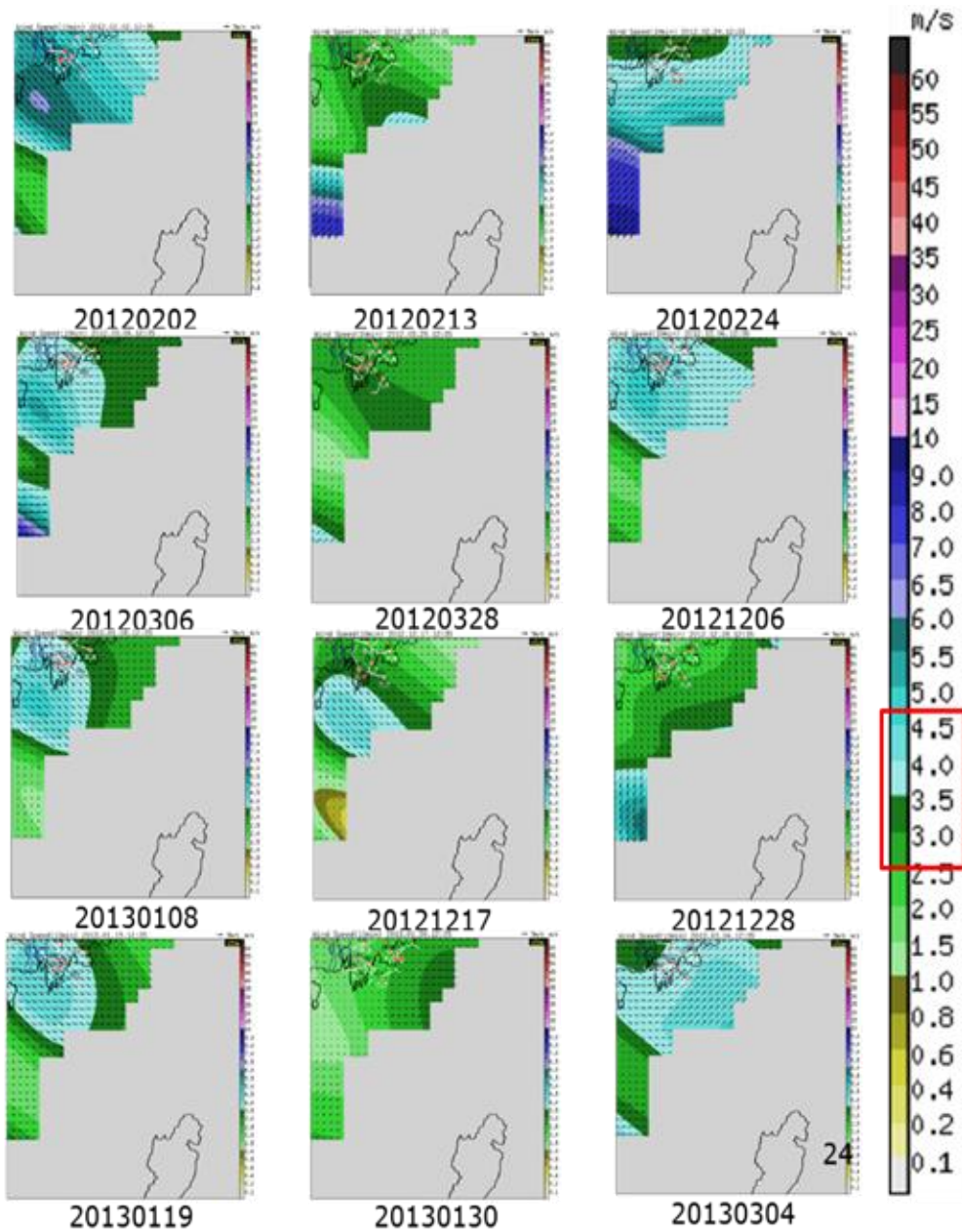


Figure 3-3 Wind speeds at the time of TanDEM-X acquisition (Source: AWS, www.kma.go.kr).

3.3 Method

With respect to automatic detection the ship and wake, the CNN algorithm that learned from the ship and wake training set data was applied to the TanDEM-X SLC image (Appendix B). By automatically selecting the ship and wake, I calculated the azimuthal distance between the detected ship and wake by using edge filtering and Radon transform. The precise direction and location of the intersection of the linear wake component were calculated from Radon transform to calculate the azimuth offset at a high resolution within a subpixel. The subpixel distance of azimuth offset can be converted to the ground velocity. Furthermore, ATI compared to the ship velocity extracted from the azimuth offset was generated by using the TerraSAR-X and TanDEM-X pairs. Land masking was conducted by using a SRTM DEM with a 30-m spatial resolution. The generated ATI phase can be expressed at the wrapped velocity within the velocity range response to the along-track baseline. The ship velocity was compared to in-situ data such as projected ground velocity using AIS (Figure 3-4). The azimuth offset using Radon transform and the ATI algorithm are further discussed in the following sections.

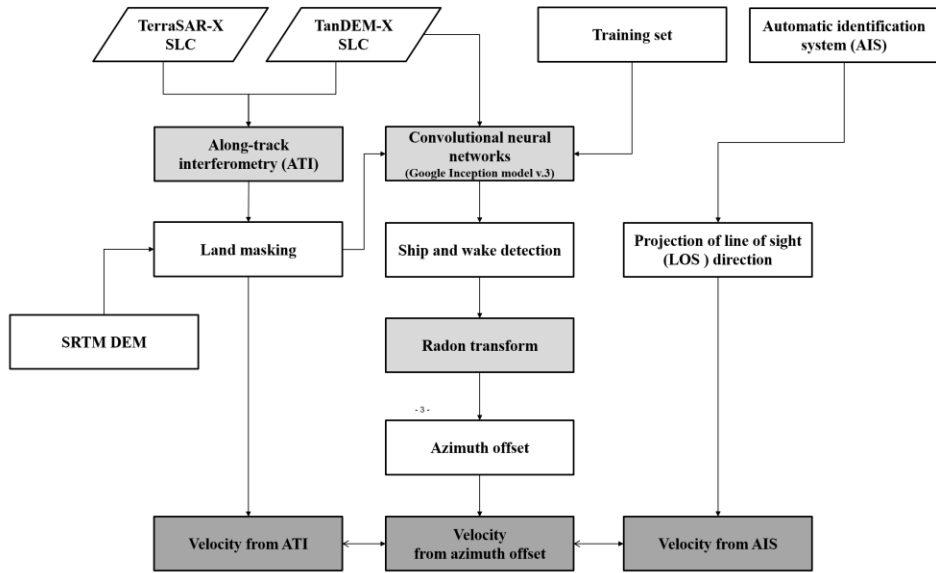


Figure 3-4 Flowchart for calculating a ship velocity using TanDEM-X data from convolutional neural networks

3.3.1 Azimuth offset calculated from Radon transform

Radon transform was applied to determine the location of ship and wake images resulting from the CNN. The technique conducts line integrals on two-dimensional images, and accumulates points integrated on the Radon transform space. It is an effective method to highlight and detect linear features such as ship wakes. It is also extremely effective for feature extraction on images wherein relevant features cannot be easily distinguished from clutter due to the unique integral function. The Radon transform conversion equation for $f(x, y)$ of a 2-dimensional image is given as follows:

$$\begin{aligned} & \int \int_{-\infty}^{\infty} f(x, y) \delta(x \cos \theta + y \sin \theta) dx dy \\ & -\infty < x < \infty \\ & -\infty < y < \infty \\ & -\infty < \rho < \infty \\ & 0 \leq \theta < \pi \end{aligned} \tag{3-4}$$

Wake patterns of ships observed in images are classified into turbulent wake, one narrow-V wake, and Kelvin arm. The wakes are simply represented with one straight line or two in most cases. Edge filtering of a wake is performed to highlight the line features in the amplitude image. Thus, stronger signals are observed on the Radon

domain when the linear characteristics are stronger. With respect to the edge detection of SAR images, the brightness values of each pixel are input for $f(x, y)$. The accumulation of a normal length that represents the distance between wake rotation components and the starting point of the image on the Radon domain is shown in Figure 3-5. The linear component of the detected ship wake edge is denoted as L , and x' represents the minimum distance between the origin point of an image and a linear component (L).

The linear component is defined by locating the two peaks in the Radon transform domain. It is possible to define the linear component generated by the ship wake in the SAR amplitude image by using the minimum distance and the rotation angle. The intersection point of the V-wake pattern is estimated using the azimuthal distance of the subpixel from the starting point of the image x' and direction θ . The minimum distance can be defined by the azimuth offset distance. The azimuth offset can be used for the intersection of the two linear components generated by the wake and the position of the subpixel corresponding to the latitude and longitude of the ship. It is possible to estimate the subpixel distance along the azimuth direction between the starting point of intersection from wake and the end point of the ship.

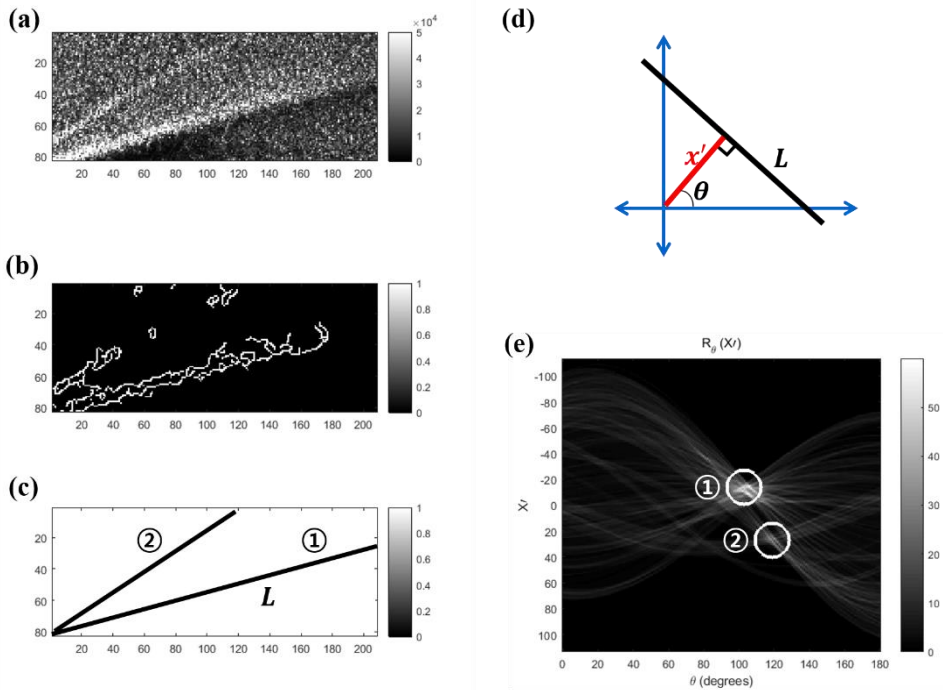


Figure 3-5 (a) TanDEM-X amplitude image detected from wake; (b) edge detection from amplitude image; (c) the linear component from Radon transform; (d) definition of Radon transform on a two-dimensional image; and (e) wake features expressed on the Radon domain.

According to the derived equation in “1.2 Background of Doppler parameter” section, the ship velocity is calculated as follows:

$$V_{ship} = \frac{V_{sat} A_{offset}}{\cos(\theta_{in}) R_{slant}} \quad (3-5)$$

where V_{sat} denotes satellite velocity, A_{offset} denotes the azimuth offset, θ_{in} denotes the local incidence angle, and R_{slant} denotes the slant range distance. The velocity of a ship can be estimated by calculating the distance of azimuth offset. Figure 3-6 shows an example of the azimuth offset distance between a detected ship and its wake in an SAR image.

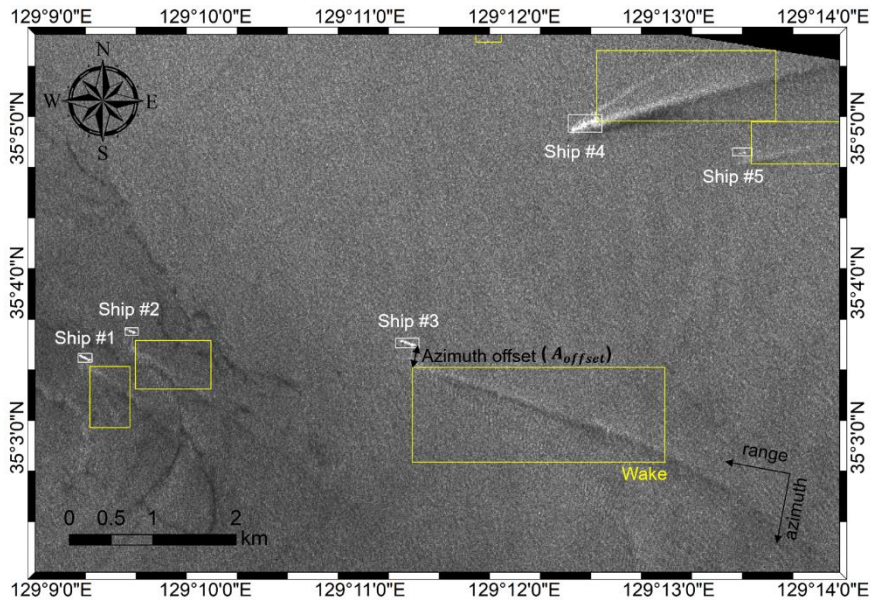


Figure 3-6 Example of azimuth offset between the detected ship and wake

3.3.2 Along-track interferometry

Along-track interferometry (ATI) techniques are based on simultaneous acquisition of two SAR images from separate antennas. The ATI phase is proportional to the Doppler shift effect of the backscattered signal, and is thus related to the radial velocity of the moving target. Following the initial publication of this technique, the ATI-SAR was initially demonstrated with the Shuttle Radar Topography Mission (SRTM) [Romeiser et al., 2005]. The TanDEM-X mission was launched in 2010, and several studies utilized interferometry with TanDEM-X. Its primary goal is the acquisition of a high-precision digital elevation model (DEM) from across-track interferometry (XTI). The two satellites of the formation, TerraSAR-X and TanDEM-X, are flown in a helical orbit that allows for safe and flexible adjustment of the XTI/ATI baselines. Thus, sensitivities to elevation changes and to moving targets are selected over a wide range [Suchandt and Runge, 2015]. The TanDEM-X mission can provide very sensitive measurements of moving targets, such as ships and tidal currents, due to the relatively longer along-track baseline between TerraSAR-X and TanDEM-X. This is advantageous over other methods due to its high sensitivity to moving targets and flexible along-track baseline.

Moving target velocity in the sea is estimated by using this technique by converting the interferometric phase of ATI-SAR to velocity after removing the flat Earth phase as well as the phase from the across-track direction. However, a baseline of TanDEM-X data consists of both along-track and across-track directions, and information in

the across-track direction must be eliminated for an appropriate interpretation. This should be considered for TanDEM-X data acquisition of moving target velocity [Kang and Kim, 2013]. The contributions of the two components to the interferometric phase are as follows:

$$V_{\text{ATI}} = \frac{V_{\text{sat}} \phi_{\text{ATI}}}{2 k_e B_{\text{ATI}} \sin\theta_I} \quad (3-1)$$

$$H_{\text{XTI}} = \frac{V_{\text{sat}} \phi_{\text{XTI}}}{2 k_e B_{\text{XTI}} \sin\theta_I} \quad (3-2)$$

where V_{ATI} and H_{XTI} denotes the moving target velocity and the elevation change, respectively, V_{sat} denotes the satellite velocity, ϕ_{ATI} denotes the phase of ATI-SAR, B_{ATI} denotes the along-track baseline, B_{XTI} denotes the across-track baseline, and θ_I denotes the angle of incidence. The extracted velocity of ATI-SAR should be projected in the LOS direction.

The wrapped velocity of ships was acquired by using ATI. The velocity of a ship is expressed as follows:

$$V_{ship} = \phi_{ATI} + N_{amb} V_{ran} + error \quad (3-3)$$

where V_{ship} represents the velocity in the LOS direction, ϕ_{ATI} denotes the ship velocity from ATI phase, N_{amb} denotes the ambiguity velocity, V_{ran} denotes the velocity range based on the ATI baseline of TanDEM-X, and $error$ denotes the error according to the XTI phase. Additionally, the fixed land phase was eliminated from the image for the relative moving velocity when compared to topography.

3.4 Result and discussion

The pairs of 12 CNN-processed TanDEM-X scenes of the Korea Strait and their respective ship and wake detection results are shown in Figure 3-7, 3-8, and 3-9. The detection performance was sufficiently suitable to clearly distinguish ships and wakes. In a quantitative accuracy test, the results were compared to AIS data acquired at the same time period as the SAR images as described in Appendix B.

Automatic detection of ships and wakes was employed using the CNN-based Google Inception v.3 model, which is a deep learning technique. Compared to the AIS data, the ship detection accuracy was 91.0%, and that of the wake was 93.2%. Although the ship and wake detection performance was excellent, the number of detected wakes was relatively small because slowly moving ships do not always appear clearly on SAR images, depending on the ship movement. A ship with a low velocity of less than approximately 1 m/s was not detectable because a wake did not occur.

When both ships and wakes were well-detected, the direction and location of ships and wakes were accurately identified by using a Radon transform to calculate the azimuth offset, which was then used to determine the position of the wake from subset data using a CNN. Ship velocity in the LOS direction was calculated by using the azimuth offset and compared to AIS data projected in the LOS direction.

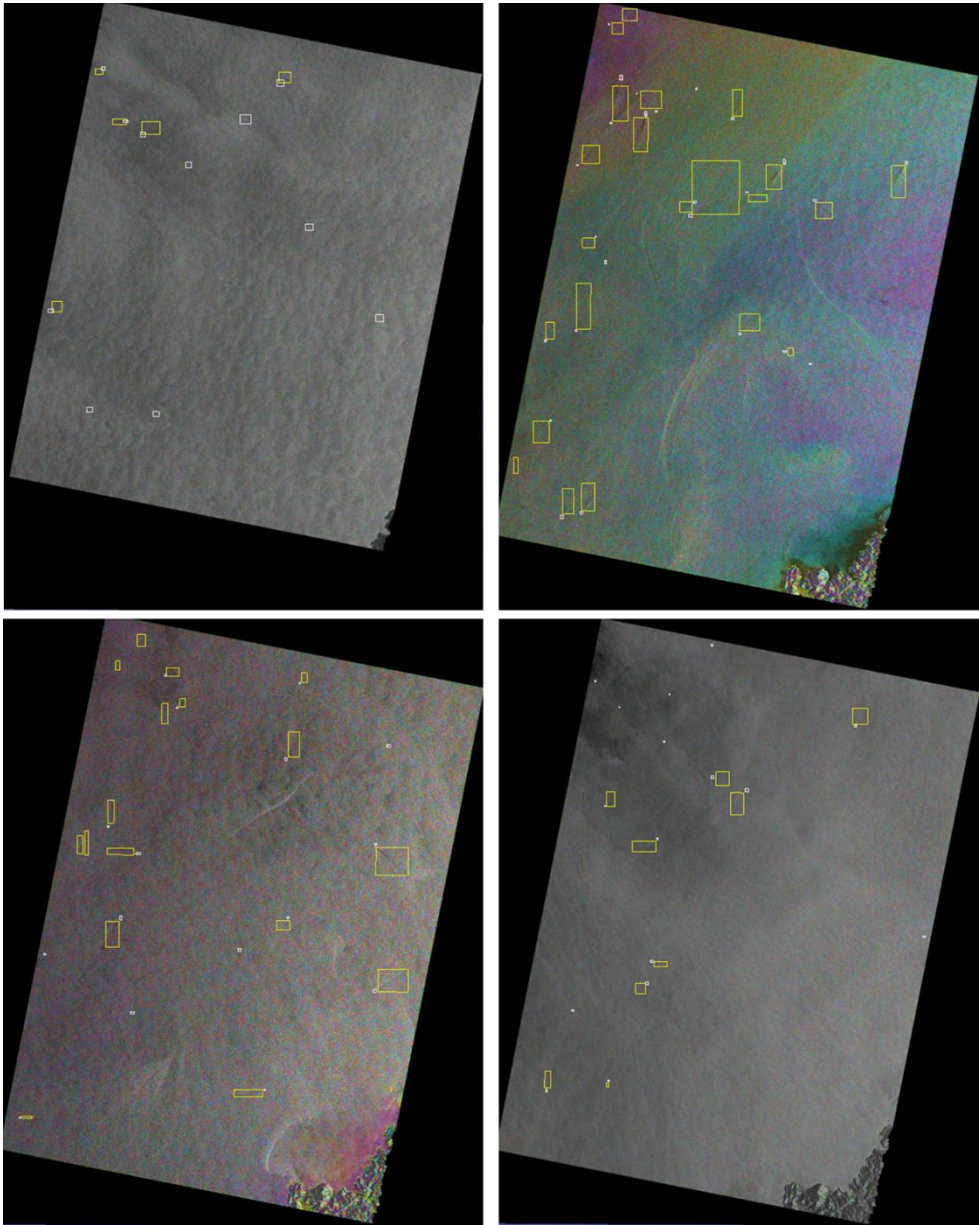


Figure 3-7 Result of ship and wake detection from convolutional neural networks (TanDEM-X data acquired on 2012-02-02, 2012-02-13, 2012-02-24, and 2012-03-06)

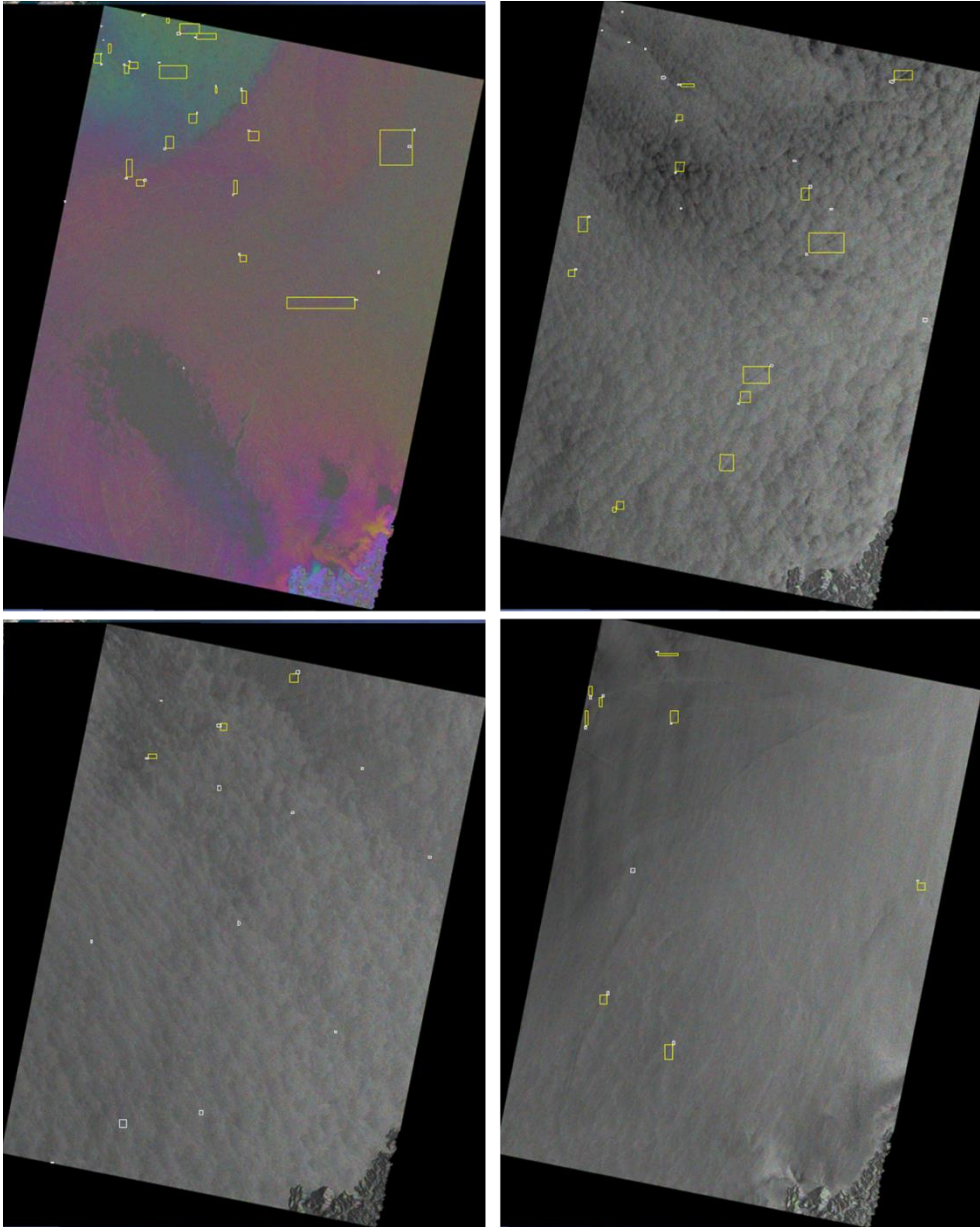


Figure 3-8 Result of ship and wake detection from convolutional neural networks (TanDEM-X data acquired on 2012-03-28, 2012-12-06, 2012-12-17, and 2012-12-28)

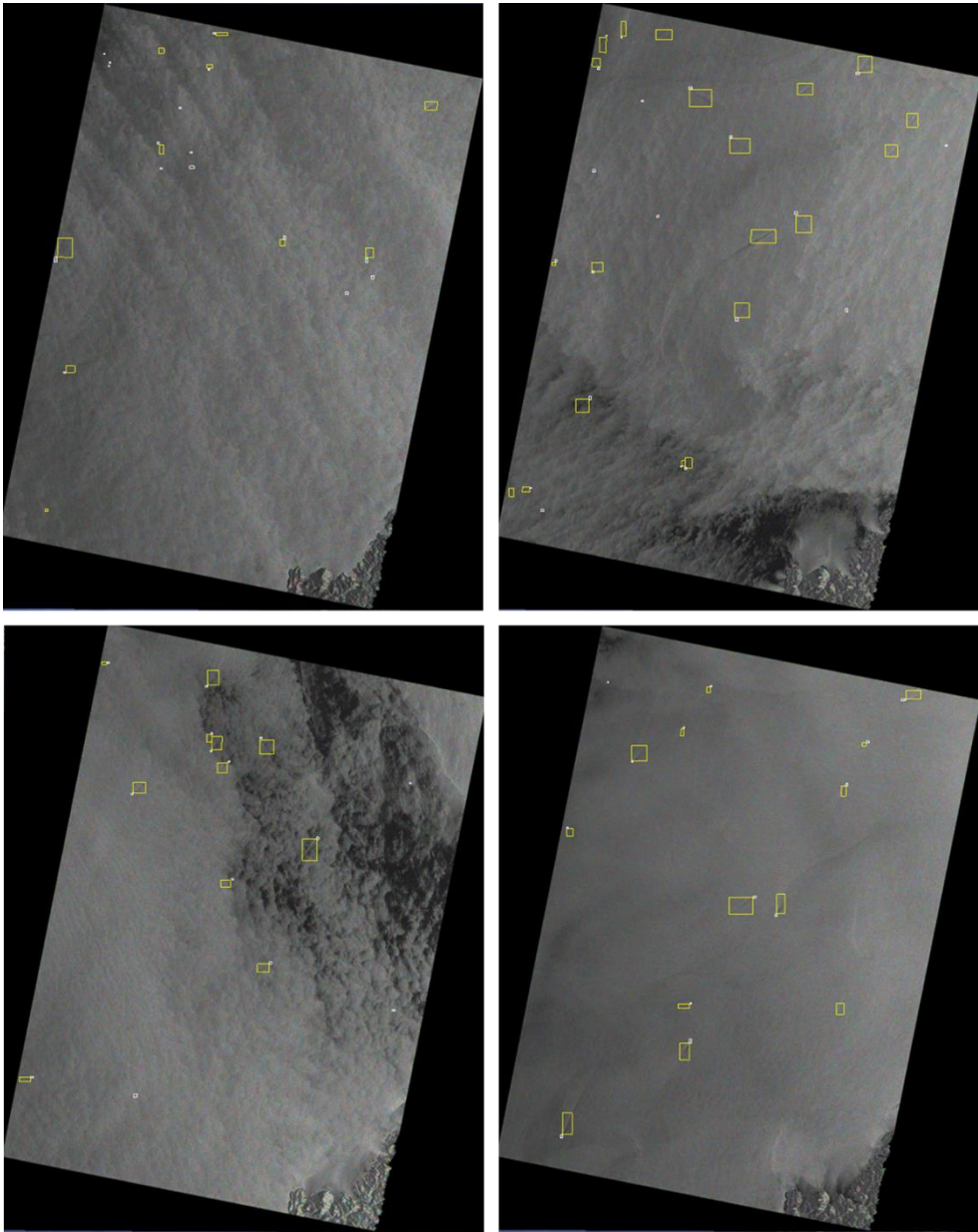


Figure 3-9 Result of ship and wake detection from convolutional neural networks (TanDEM-X data acquired on 2013-01-08, 2013-01-19, 2013-03-04, and 2013-03-15)

The comparison results of ship velocities are summarized in Table 3-3. The mean difference between the ship velocity using the azimuth offset and the ship velocity using AIS data is less than 0.13 m/s. Although the number of comparison points is limited, the R-square of 0.99 indicated a close fit to the data, and the RMSE was 0.16 m/s. The ship velocity determined using the azimuth offset was strongly correlated with the ship velocity determined using the AIS data. Additionally, the ship velocity calculated by the ATI phase was also compared to the ship velocity from the AIS data. The comparison results indicate that the R-square is 0.98 and the RMSE is 0.55 m/s (Figure 3-10). The velocity was only compared when both the ship and wake are detected, and the numbers are less than the ship velocity calculated by ATI although the accuracy is slightly higher. This is because the ship and wake are well detected in the single SAR amplitude image, and it can be converted to the correct speed if the position is accurately calculated.

The reason for the high RMSE of ATI is because the ATI phase calculated by TerraSAR-X and TanDEM-X includes the along-track baseline and also the across-track baseline. While calculating sea surface current, across-track effects are negligible because the ocean surface is flat and wave height-induced phase variations are low [Suchandt and Runge, 2012]. However, tall ships may induce errors in the phase since remaining XTI components exist. The XTI baseline of target objects with high structures, such as ships, is still present. If the XTI phase of a ship can be estimated by a model that calculates ship heights, then it is possible to estimate the ship velocity with increased accuracy by using TanDEM-X ATI data.

Figure 3-11 shows the along-track baseline with respect to the latitude. The along-track baseline of TanDEM-X must be below 100 m to maintain high coherence. The along-track baselines (in the blue boxes) are located at mid latitudes. Our study site corresponds to the Korea Strait that lies at 35°N, and the corresponding along-track baselines are approximately 127–349 m. The detectable velocity range is 0.94–2.62 m/s (Figure 3-12). After eliminating the XTI phase, the ATI phase of TanDEM-X from the flexible along-track baseline and the high sensitivity to moving targets offers new possibilities for velocity measurements using ATI techniques.

Table 3-3 Accuracy of ship velocity from azimuth offset compared to AIS

# of Ship	Azimuth offset from Radon transform (m)	Ship velocity from azimuth offset (m/s)	Ship velocity from ATI phase (m/s)	Ship velocity from AIS (m/s)
Ship #1	90	-2.68	-2.37	-2.79
Ship #2	210	-6.27	-7.64	-6.37
Ship #3	261	-7.79	-8.69	-7.69
Ship #4	157	-4.69	-4.51	-4.91
Ship #5	162	-4.83	-4.55	-5.19

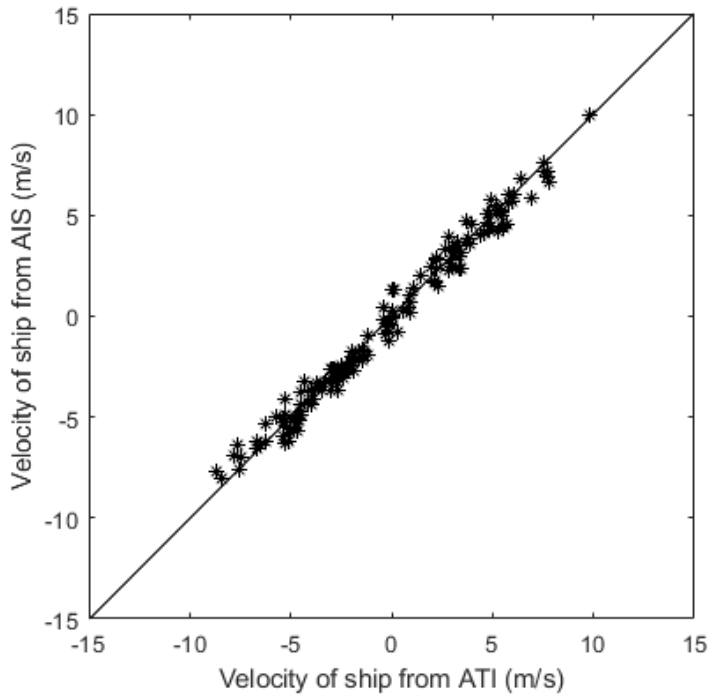


Figure 3-10 Ship velocity from ATI compared to AIS data projected LOS direction

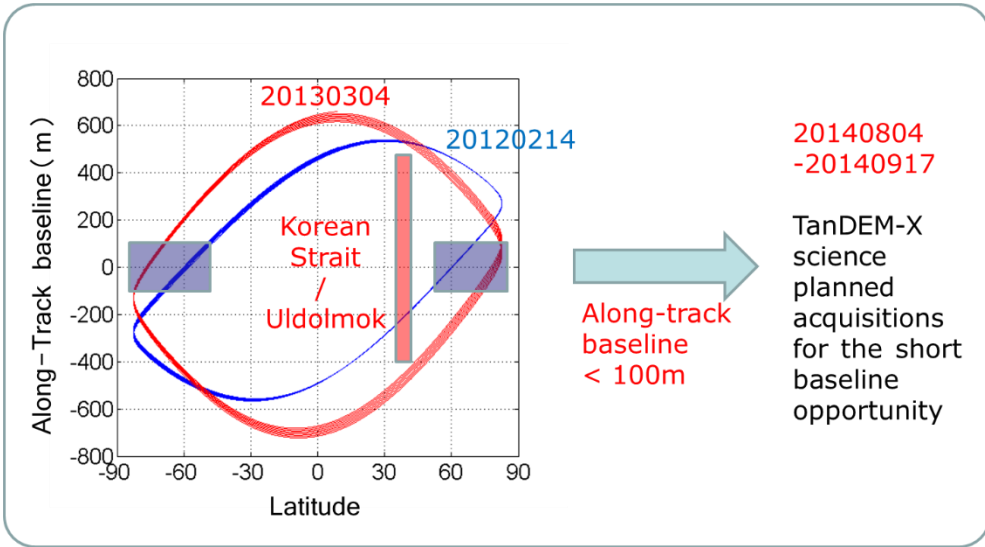


Figure 3-11 TanDEM-X orbit geometry

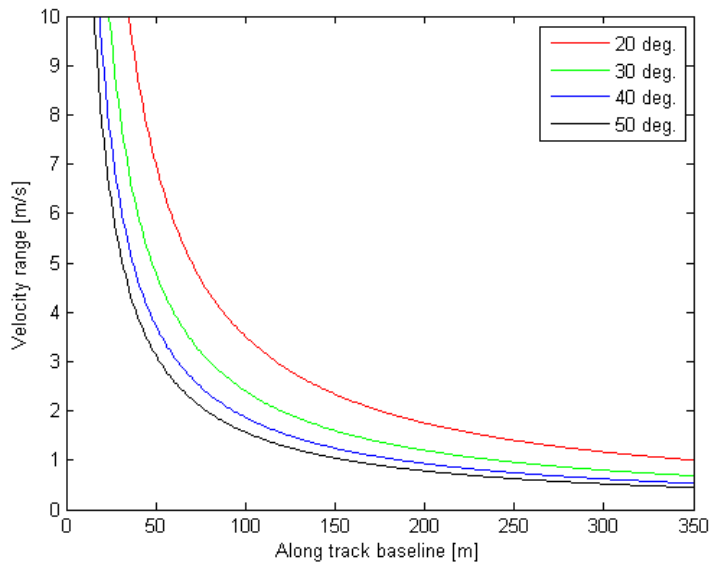


Figure 3-12 Velocity range response to along-track baseline

4 Conclusion

By using Doppler parameters, I retrieved the distributed target using SAR raw data and the artificial target velocity using SAR SLC data of a single channel SAR system. First, I retrieved the Doppler velocities of five tropical cyclones using RADARSAT-1 ScanSAR raw data under extreme conditions. The results obtained from the SAR raw data demonstrate the possibility of applying this technique to characterize the sea surface responses to tropical cyclones. The derivable characteristics are the hurricane's eye size and spatial variations in surface velocities in the center of a hurricane. In order to obtain these characteristics under hurricane conditions, which have been rarely studied, an accurate assessment of Doppler velocities is required. I applied several challenging approaches to calculate the Doppler velocities from RADARSAT-1 ScanSAR data. RADARSAT-1's orbit and attitude information are not accurate enough for direct Doppler centroid determination, and thus the calculation of the predicted Doppler centroid requires a number of corrections and improvements. I used an established model with improved parameters (including slant range distance, look angle, and hour angle), adjusted ACCC method, and iterative fitting procedure. The fitting procedure included a global fitting method and an attitude control algorithm for correct biases. Although I obtained relatively accurate Doppler velocities by improving the parameters, there should be careful consideration of the actual meaning of Doppler velocities, particularly in hurricane-generated seas. According to the derivation of Doppler velocities for wind-generated

seas, “velocity bias” is the dominant contributor to Doppler velocity. The bias is caused by wind-induced waves via the correlation between orbital motions and their modulated radar cross sections. However, hurricane-generated winds (revolving in a vortex system) and the generated waves’ response (propagation direction) to the winds may be different from ordinary wind conditions. Additional calculations of Doppler velocities using hurricane data and investigations of their characteristics are necessary to understand the behavior and velocities of ocean waves under extreme conditions. In this respect, our study was the first attempt to characterize Doppler velocities influenced by tropical cyclones using different and sequential RADARSAT-1 ScanSAR data. Although the number of comparison points was limited, the comparison of the results with in-situ measurements of drift buoys also support this finding.

Second, the ships and wakes were detected using the CNN-based Inception v.3 model, which is a deep learning technique, from TanDEM-X SLC data. Compared to the AIS information, the accuracy of ship detection was 91.0% and that of the wakes was 93.2%. Although the ship and wake detection performance was excellent, the number of wake detections was relatively small because slowly moving ships do not always appear clearly on SAR images, depending on the direction of ship movement. When both ships and wakes were well-detected, the azimuth offset between the ships and wakes was calculated using Radon transformation. The ship velocity determined using azimuth offset was strongly correlated with the ship velocity determined using AIS data. Although the number of comparison points is limited, the R-square value was 0.99, which indicates a close fit to the data, and the RMSE was 0.16 m/s. Further,

the velocity from ATI using TanDEM-X was calculated and compared to the velocity from AIS. The R-square value was 0.98 and RMSE was 0.55. Although the number of verifications was small, the velocity estimated from the azimuth offset was slightly more accurate than that from ATI. This is because XTI phase components were still present in the interferometric phase because TanDEM-X pairs were used. Errors may be negligible when estimating sea surface current; however, they may not be negligible when estimating ship velocity with a high structure due to the residual XTI phase. If an accurate ship XTI phase can be estimated through improved ship modelling, it will be possible to estimate the ship velocity with greater accuracy.

Both techniques were applied and an attempt was made to validate them with in-situ observations, such as buoy and AIS data, in order to evaluate their feasibility. The result shows that the TDX ATI has a high potential to provide precise velocities, but it requires to have a short along-track baseline (less than 100 m) to achieve significant coherence. Most of our ATI pairs have very long along-track baselines and the results were not satisfactory. In the case of ATI pairs with long-baselines, Doppler centroid measurements using SAR raw data and azimuth offset using SAR SLC data from a single SAR system is useful. Based on the products of SAR, I could extract a distributed target velocity such as a sea surface current velocity using SAR raw data and artificial target velocity such as a ship using SAR SLC data can be estimated. Thus, the estimation of Doppler parameters, such as Doppler centroid measurements, azimuth offset, and ATI, can lead to the effective extraction of velocity in various applications including sea surface current and ship velocity.

Appendix A. Detailed derivation of Doppler velocity during tropical cyclones

The detailed derivation of Doppler velocity is given well by [Chapron et al., 2005].

According to their model, the line-of sight Doppler velocity is expressed by

$$\bar{c} = \int c(\vec{k})\Lambda(\vec{k})d\vec{k} / \int \Lambda(\vec{k})d\vec{k}. \quad (\text{A1})$$

Because a pure Bragg condition could yield for \bar{c} a weighted mean of the phase velocity of the resonant scales. In ocean surface, these short-scale Bragg resonant scales are overlaid on longer surface waves, which can be changed from the value when they are on a flat surface ($\vec{k}_b = k_e \sin \theta$). So the distribution function, Λ , can be written by

$$\Lambda(\vec{k}) = \left[\frac{\sigma_0(\vec{k})}{\sigma_0(k_b)} \right] P(\vec{k}). \quad (\text{A2})$$

where, P is the distribution function for the resonant conditions, and deduced from the probability distribution function of the longer wave slopes. These models correspond to rigid longer tilt modulations. If I extend the distribution to a real ocean conditions (longer waves are moving), I should consider the orbital velocities and vertical accelerations of the larger scale components. That is,

$$\Lambda(\vec{k}, \vec{\eta}, \vec{\ddot{\eta}}) = \left[\frac{\sigma_0(\vec{k})}{\sigma_0(k_b)} \right] P(\vec{k}, \vec{\eta}, \vec{\ddot{\eta}}). \quad (\text{A3})$$

where $\vec{\eta}$ and $\vec{\ddot{\eta}}$ are the local (horizontal and vertical) velocity and acceleration, respectively. Thus, the mean line-of-sight Doppler velocity becomes

$$\bar{c} = \frac{\iiint c(\vec{k}, \vec{\eta}, \vec{\ddot{\eta}}) \left[\frac{\sigma_0(\vec{k})}{\sigma_0(k_b)} \right] P(\vec{k}, \vec{\eta}, \vec{\ddot{\eta}}) d\vec{k} d\vec{\eta} d\vec{\ddot{\eta}}}{\iiint \left[\frac{\sigma_0(\vec{k})}{\sigma_0(k_b)} \right] P(\vec{k}, \vec{\eta}, \vec{\ddot{\eta}}) d\vec{k} d\vec{\eta} d\vec{\ddot{\eta}}}. \quad (\text{A4})$$

By analogy, the mean scatter velocity \bar{c} could be called “velocity bias,” and \bar{c} includes biases due to tilt and hydrodynamic modulations of the radar cross section.

This equation is quite difficult to interpret. Thus, without specifying the details of the backscatter from the sea surface, and employing a two-scale approach in which the radar cross section can be defined over a collection of rough facets, then

$$\bar{c} = \frac{\overline{(u \sin \theta_i - w \cos \theta_i) \sigma_0(\theta_i + \Delta\theta)}}{\overline{\sigma_0(\theta_i + \Delta\theta)}} \quad (\text{A5})$$

where, u and w are the horizontal (in the range direction) and vertical velocities of the surface elements. Here, $\Delta\theta$ (the local modification of the incidence angle, θ_i) can be expressed using the wave slope and the surface elevation (η):

$$\Delta\theta = -\frac{\partial\eta}{\partial x} + \frac{1}{2 \tan \theta_t} \left\{ [1 + \sin \theta_t] \left(\frac{\partial\eta}{\partial x} \right)^2 + \left(\frac{\partial\eta}{\partial y} \right)^2 \right\} \quad (\text{A6})$$

Ignoring hydrodynamic modulations of the roughness,

$$\sigma_0(\theta_t + \Delta\theta) = \overline{\sigma_0} + \Delta\theta \frac{\partial\sigma_0}{\partial\theta} + \frac{\Delta\theta^2}{2} \frac{\partial^2\sigma_0}{\partial\theta^2}. \quad (\text{A7})$$

If I assume that there is a monochromatic wave of amplitude a , wave number (k_x , k_y), intrinsic radian frequency, ω , and phase,

$$\phi = [k_x x + k_y y - (k_x U_{cx} + k_y U_{cy} + \omega)t], \quad (\text{A8})$$

then,

$$\eta = a \cos \phi + A_2 \sin(2\phi) + \varepsilon_1 \quad (\text{A9})$$

$$w = a\omega + \sin \phi + W_2 \sin(2\phi) + \varepsilon_2 \quad (\text{A10})$$

$$u = U_{cx} + \frac{1}{2}U_{xx} + a\omega \cos \phi + U_2 \cos(2\phi) + \varepsilon_3 \quad (\text{A11})$$

where, U_c and U_s are quasi-Eulerian current and Stokes drift, respectively.

According to linear dispersion relation,

$$\omega^2 = gk \tanh(kH) \quad (\text{A12})$$

and,

$$U_{sx} = a^2 k_x \omega \frac{\cosh(2kH)}{2 \sin^2(kH)} + \varepsilon_4 \approx k_x \omega a^2 (kH \gg 1) \quad (\text{A13})$$

Now, I replace the above Doppler velocity equation with relevant equations, then,

$$\bar{V} = U_{sx} \cos \theta_l \frac{1}{\hat{\sigma}_0} \frac{\partial \sigma_0}{\partial \theta} + \left[U_{cx} + \frac{1}{2} U_{sx} \right] \sin \theta_l + \varepsilon, \quad (\text{A14})$$

and the horizontal Doppler velocity (V_s) is,

$$V_s = \frac{U_{sx}}{2 \tan \theta_l} \frac{1}{\hat{\sigma}_0} \frac{\partial \sigma_0}{\partial \theta} + \left[U_{cx} + \frac{1}{2} U_{sx} \right]. \quad (\text{A15})$$

As shown in equation A15, the Doppler velocity retrieved from RADARSAT-1 SAR data includes additional velocities (or ‘velocity bias’) due to the nonlinearity of surface waves (resonant capillary and longer oceanic waves) as well as surface current. The additional velocities can be dominated when the ocean surface waves

propagate in the LOS direction, and can increase the nonlinearity. But under the hurricane conditions, the surface waves can propagate in uni-direction or radial directions rather than propagate in the local wind direction according to the studies [Johannessen et al., 2008; Ochi, 2003; King and Shemdin, 1978; Young, 2006] (Figure A-1). In these cases, the nonlinearity cannot be significant, and thus the Doppler velocity can be much closer to the surface current.

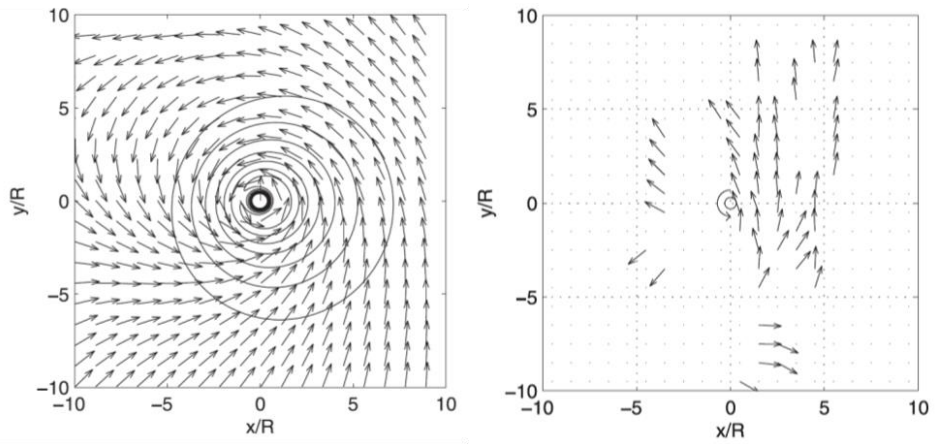


Figure A-1 Wind (left) and wave (right) directions under hurricane conditions. These figures were taken from [Young, 2006].

Appendix B. Convolutional neural networks for detecting ship and wake using SAR SLC data

Deep learning is a type of machine learning that extracts data features, then detects and classifies them through an advanced abstraction of learned data by using various nonlinear conversion techniques. A Convolutional Neural Network (CNN) is a deep learning technique that is frequently used for image-based feature extraction or classification. Improved CNN techniques were recently introduced at the international visual recognition contest ImageNet Challenge and attract increasing attention for their high accuracy [Krizhevsky et al., 2012]. The CNN is a supervised learning of numerous training set data; and it is a process of determining the weight value of each function and outputting results. The CNN applies convolution to neural networks. A filter operation is typically applied to images to extract specific features, and low-dimensional information is scaled up to a higher dimension to facilitate the classification of training sets. The CNN consists of a convolution layer, pooling layer, and fully connected layer as shown in Figure B-1. I move the kernel learned from input data coming in from the previous layer to the next one, and the convolution layer conducts convolution operations by considering image features and extracting features to produce a feature map. In the process, multiple convolution layers are produced to construct a deep network, and the data set undergoes a pooling process to downsize image dimensions. Pooling is a subsampling process of pixel values that uses various dimension reduction methods since the values of adjacent pixels can be

very similar to one another. At this stage, maxpooling is applied in most cases to improve the extraction of features. Repeated operations of convolution and pooling automatically generate features based on the values of filter weights, and targets are detected based on this information. With respect to architectures scaled up based on CNN, the Inception v3 by Google is a representative model of image classification and detection [Szegedy et al., 2016]. This model can detect, classify, and learn targets from images and is currently available to internet users as an open source platform. Although the function is not easy to perform due to its highly complicated architecture, it realizes tasks in TensorFlow via Python programming language, and the results can be modified based on various objectives. In the study, TanDEM-X amplitude images were used as input data, and ship and wake training set data were generated for learning purposes. Training set data were selected by learning with more than 20 regions of interest (ROIs). In the training set data, the ship was generated based on real ship data. With respect to the wake pattern, training set data from the starting point to the end point were selected for learning. Ships and wakes were detected from each of the 12 SAR scenes based on the learned data.

Table B-1 shows the AIS comparison and accuracy test results. Table B-1 represents the number of ships recorded by AIS with the number of ships detected by CNN and the number of ship detection and wakes generated by ship movements. The accuracy represents ship detection rate in reference to AIS, thereby indicating the accuracy of wake detection among ships detected by CNN. The ship detection rate of the 12 scenes in reference to AIS demonstrates a high accuracy of 91.0%. The wake

detection rate based on interpreted ships reached 93.2% accuracy. This is potentially because ships stopped or moved very slowly, and the wake pattern was relatively invisible to SAR imaging. In this case, targeted objects were not undetected (Figure B-2).

Although the detection rate was high in general, the data collected on December 17, 2012 indicated a ship detection rate of 68.4% and a wake detection rate of 60.0%. The aforementioned rates are low when compared to those of other data sets. Given the weather conditions on that particular day, ships and wakes were not accurately detected because the wind speed was 7.9 m/s, and the backscattering coefficient increased due to the rough ocean surface.

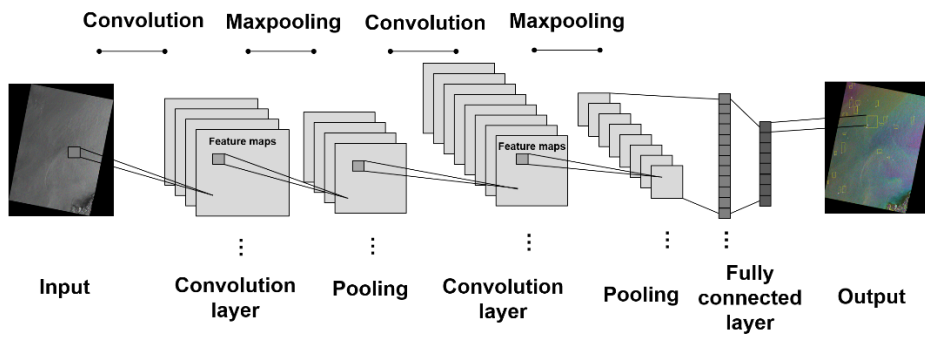


Figure B-1 Convolutional Neural Networks for ship and wake detection

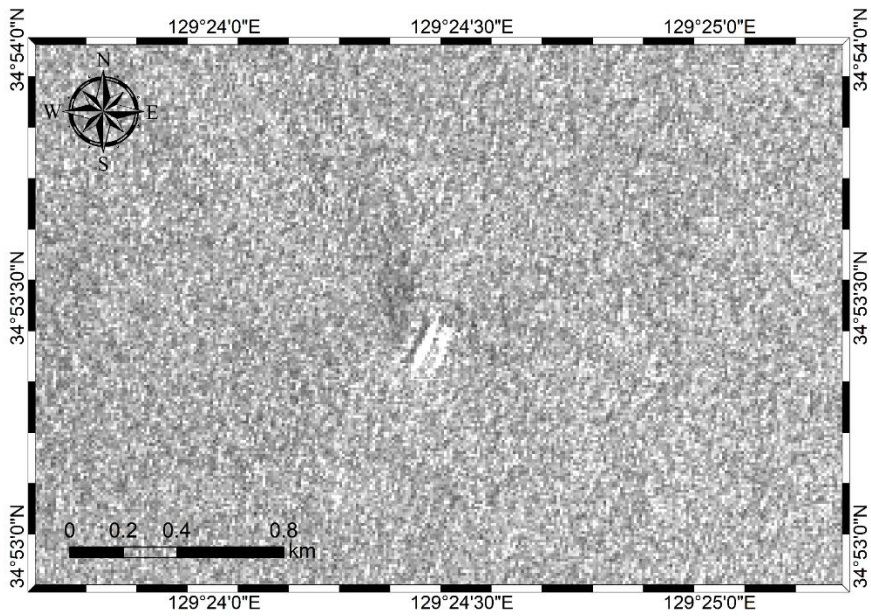


Figure B-2 Example of undetected wake using CNN, wake pattern was relatively invisible to SAR imaging.

Table B-1 Accuracy assessment of ship and wake detection compared to AIS

Time UTC	AIS(ship)	CNN(ship)	Man(wake)	CNN(wake)	Accuracy	Accuracy
					(ship)	(wake)
2012-02-02T21:35:46	12	11	6	5	91.7	83.3
2012-02-13T21:35:46	25	24	22	20	96.0	90.9
2012-02-24T21:35:46	13	13	11	11	100.0	100.0
2012-03-06T21:35:46	14	13	7	7	100.0	100.0
2012-03-28T21:35:47	22	18	17	15	81.8	88.2
2012-12-06T21:35:53	15	15	11	10	100.0	90.9
2012-12-17T21:35:52	19	13	5	3	68.4	60.0
2012-12-28T21:35:52	8	8	7	7	100.0	100.0
2013-01-08T21:35:52	14	14	8	8	100.0	100.0
2013-01-19T21:35:51	19	18	16	15	94.7	93.75
2013-03-04T21:35:51	12	12	11	11	100.0	100.0
2013-03-15T21:35:52	16	13	12	12	81.25	100.0
Total	189	172	133	124	91.0	93.2

References

- Alpers, W., & Hennings, I. (1984). A theory of the imaging mechanism of underwater bottom topography by real and synthetic aperture radar. *Journal of Geophysical Research: Oceans*, 89(C6), 10529-10546.
- Budillon, A., Pascazio, V., & Schirinzi, G. (2008). Estimation of radial velocity of moving targets by along-track interferometric SAR systems. *IEEE Geoscience and Remote Sensing Letters*, 5(3), 349-353.
- Copeland, A. C., Ravichandran, G., & Trivedi, M. M. (1995). Localized Radon transform-based detection of ship wakes in SAR images. *IEEE Transactions on Geoscience and Remote Sensing*, 33(1), 35-45.
- Chapron, B., Collard, F., & Ardhuin, F. (2005). Direct measurements of ocean surface velocity from space: Interpretation and validation. *Journal of Geophysical Research: Oceans*, 110(C7).
- Cumming, I. G. (2004). A spatially selective approach to Doppler estimation for frame-based satellite SAR processing. *IEEE Transactions on Geoscience and Remote Sensing*, 42(6), 1135-1148.
- Cumming, I. G., & Wong, F. H. (2005). Digital processing of synthetic aperture radar data. Artech house, 1(2), 3.
- Eldhuset, K. (1996). Accurate attitude estimation using ERS-1 SAR raw data.

International Journal of Remote Sensing, 17(14), 2827-2844.

Eldhuset, K. (1996). An automatic ship and ship wake detection system for spaceborne SAR images in coastal regions. *IEEE transactions on Geoscience and Remote Sensing*, 34(4), 1010-1019.

Emanuel, K. (2005). Increasing destructiveness of tropical cyclones over the past 30 years. *Nature*, 436(7051), 686.

Fiedler, H., Boerner, E., Mittermayer, J., & Krieger, G. (2005). Total zero Doppler steering-a new method for minimizing the Doppler centroid. *IEEE Geoscience and Remote Sensing Letters*, 2(2), 141-145.

Friedman, K. S., & Li, X. (2000). Monitoring hurricanes over the ocean with wide swath SAR. *Johns Hopkins APL Technical Digest*, 21(1), 80-85.

Graber, H. C., Thompson, D. R., & Carande, R. E. (1996). Ocean surface features and currents measured with synthetic aperture radar interferometry and HF radar. *Journal of Geophysical Research: Oceans*, 101(C11), 25813-25832.

Graziano, M. D., Rufino, G., & D'Errico, M. (2014, October). Wake-based ship route estimation in high-resolution SAR images. In *SAR Image Analysis, Modeling, and Techniques XIV* (Vol. 9243, p. 92430T). International Society for Optics and Photonics.

Graziano, M. D., D'Errico, M., & Rufino, G. (2016). Wake component detection in X-band SAR images for ship heading and velocity estimation. *Remote Sensing*,

8(6), 498.

Graziano, M. D., Grasso, M., & D'Errico, M. (2017). Performance Analysis of Ship Wake Detection on Sentinel-1 SAR Images. *Remote Sensing*, 9(11), 1107.

Jao, J. K. (2001). Theory of synthetic aperture radar imaging of a moving target. *IEEE Transactions on Geoscience and remote sensing*, 39(9), 1984-1992.

Johannessen, J. A., Chapron, B., Collard, F., Kudryavtsev, V., Mouche, A., Akimov, D., & Dagestad, K. F. (2008). Direct ocean surface velocity measurements from space: Improved quantitative interpretation of Envisat ASAR observations. *Geophysical Research Letters*, 35(22).

Just, D., & Schattler, B. (1992, May). Doppler-characteristics of the ERS-1 yaw steering mode. In *Geoscience and Remote Sensing Symposium, 1992. IGARSS'92. International (Vol. 2, pp. 1349-1352)*. IEEE.

Kang, K. M., & Kim, D. J. (2013). Extraction of Ocean Surface Current Velocity Using Envisat ASAR Raw Data. *Korean Journal of Remote Sensing*, 29(1), 11-20.

Kang, K. M., & Kim, D. J. (2013, July). Feasibility study on estimating sea surface currents from single (Envisat ASAR) and dual (TanDEM-X) SAR system. In *Geoscience and Remote Sensing Symposium (IGARSS), 2013 IEEE International (pp. 1274-1277)*. IEEE.

Kang, K. M., & Kim, D. J. (2015, September). Retrieval of sea surface velocity during

tropical cyclones from RADARSAT-1 ScanSAR Doppler centroid measurements. In Synthetic Aperture Radar (AP SAR), 2015 IEEE 5th Asia-Pacific Conference on (pp. 610-613). IEEE.

Kang, K. M., Kim, D. J., Kim, S. H., & Moon, W. M. (2016). Doppler velocity characteristics during tropical cyclones observed using ScanSAR raw data. *IEEE Transactions on Geoscience and Remote Sensing*, 54(4), 2343-2355.

Kang, M., Ji, K., Leng, X., & Lin, Z. (2017). Contextual region-based convolutional neural network with multilayer fusion for SAR ship detection. *Remote Sensing*, 9(8), 860.

Katsaros, K. B., Vachon, P. W., Liu, W. T., & Black, P. G. (2002). Microwave remote sensing of tropical cyclones from space. *Journal of Oceanography*, 58(1), 137-151.

Kim, D. J., Moon, W. M., Moller, D., & Imel, D. A. (2003). Measurements of ocean surface waves and currents using L-and C-band along-track interferometric SAR. *IEEE Transactions on Geoscience and Remote Sensing*, 41(12), 2821-2832.

King, D. B., & Shemdin, O. H. (1978). Radar observation of hurricane wave directions. In *Coastal Engineering 1978* (pp. 209-226).

Krieger, G., Moreira, A., Fiedler, H., Hajnsek, I., Werner, M., Younis, M., & Zink, M. (2007). TanDEM-X: A satellite formation for high-resolution SAR interferometry. *IEEE Transactions on Geoscience and Remote Sensing*, 45(11),

3317-3341.

Krizhevsky, A., Sutskever, I., & Hinton, G. E. (2012). Imagenet classification with deep convolutional neural networks. In *Advances in neural information processing systems* (pp. 1097-1105).

Li, S. (2006). Improved Doppler centroid estimation algorithms for satellite SAR data (Doctoral dissertation, University of British Columbia).

Li, X., Zhang, J. A., Yang, X., Pichel, W. G., DeMaria, M., Long, D., & Li, Z. (2013). Tropical cyclone morphology from spaceborne synthetic aperture radar. *Bulletin of the American Meteorological Society*, 94(2), 215-230.

Liu, Y., Zhang, M. H., Xu, P., & Guo, Z. W. (2017, May). SAR ship detection using sea-land segmentation-based convolutional neural network. In *Remote Sensing with Intelligent Processing (RSIP), 2017 International Workshop on* (pp. 1-4). IEEE.

Lyzenga, D. R., & Bennett, J. R. (1988). Full-spectrum modeling of synthetic aperture radar internal wave signatures. *Journal of Geophysical Research: Oceans*, 93(C10), 12345-12354.

Madsen, S. N. (1989). Estimating the Doppler centroid of SAR data. *IEEE Transactions on aerospace and electronic systems*, 25(2), 134-140.

Manore, M., DeAbreu, R., Zabeline, V., Arkett, M., & Bradley, D. (2010). The RADARSAT Constellation Mission (RCM): Extending operational marine

surveillance for environment Canada. In ASTRO Annu. Meet..

Marandi, S. R. (1998, July). Repeatability of satellite yaw and pitch measurements made based on Doppler centroid of SAR imagery. In Geoscience and Remote Sensing Symposium Proceedings, 1998. IGARSS'98. 1998 IEEE International (Vol. 5, pp. 2471-2473). IEEE.

Marghany, M. (2009, July). Finite difference model for modeling sea surface current from RADARSAT-1 SAR data. In Geoscience and Remote Sensing Symposium, 2009 IEEE International, IGARSS 2009 (Vol. 2, pp. II-487). IEEE.

Marghany, M. (2012, June). Three-dimensional coastal front visualization from RADARSAT-1 SAR satellite data. In International Conference on Computational Science and Its Applications (pp. 447-456). Springer, Berlin, Heidelberg.

Moller, D., Frasier, S. J., Porter, D. L., & McIntosh, R. E. (1998). Radar-derived interferometric surface currents and their relationship to subsurface current structure. *Journal of Geophysical Research: Oceans*, 103(C6), 12839-12852.

Mouche, A. A., Collard, F., Chapron, B., Dagestad, K. F., Guitton, G., Johannessen, J. A., ... & Hansen, M. W. (2012). On the use of Doppler shift for sea surface wind retrieval from SAR. *IEEE Transactions on Geoscience and Remote Sensing*, 50(7), 2901-2909.

Nam, S., Kim, D. J., & Moon, W. M. (2012). Observed impact of mesoscale circulation on oceanic response to Typhoon Man-Yi (2007). *Ocean Dynamics*,

62(1), 1-12.

National Oceanic and Atmospheric Administration (NOAA) National Hurricane Center (NHC) [Online]. Available: <http://www.nhc.noaa.gov/>

Ochi, M. (2003). Hurricane generated seas (Vol. 8). Elsevier.

Raney, R. K. (1986). Doppler properties of radars in circular orbits. *International Journal of Remote Sensing*, 7(9), 1153-1162.

Reppucci, A., Lehner, S., Schulz-Stellenfleth, J., & Brusch, S. (2010). Tropical cyclone intensity estimated from wide-swath SAR images. *IEEE Transactions on Geoscience and Remote Sensing*, 48(4), 1639-1649.

Rey, M. T., Tunaley, J. K., Folinsbee, J. T., Jahans, P. A., Dixon, J. A., & Vant, M. R. (1990). Application of Radon transform techniques to wake detection in Seasat-A SAR images. *IEEE Transactions on Geoscience and Remote Sensing*, 28(4), 553-560.

Romeiser, R., & Thompson, D. R. (2000). Numerical study on the along-track interferometric radar imaging mechanism of oceanic surface currents. *IEEE transactions on geoscience and remote sensing*, 38(1), 446-458.

Romeiser, R., Breit, H., Eineder, M., Runge, H., Flament, P., De Jong, K., & Vogelzang, J. (2005). Current measurements by SAR along-track interferometry from a space shuttle. *IEEE Transactions on Geoscience and Remote Sensing*, 43(10), 2315-2324.

- Romeiser, R., Suchandt, S., Runge, H., Steinbrecher, U., & Grunler, S. (2010). First analysis of TerraSAR-X along-track InSAR-derived current fields. *IEEE Transactions on Geoscience and Remote Sensing*, 48(2), 820-829.
- Romeiser, R., Runge, H., Suchandt, S., Kahle, R., Rossi, C., & Bell, P. S. (2014). Quality assessment of surface current fields from TerraSAR-X and TanDEM-X along-track interferometry and Doppler centroid analysis. *IEEE Transactions on Geoscience and Remote Sensing*, 52(5), 2759-2772.
- Scherbakov, A., Hanssen, R., Vosselman, G., & Feron, R. (1996, December). Ship wake detection using Radon transforms of filtered SAR imagery. In *Microwave Sensing and Synthetic Aperture Radar* (Vol. 2958, pp. 96-107). International Society for Optics and Photonics.
- Schwegmann, C. P., Kleynhans, W., Salmon, B. P., Mdakane, L. W., & Meyer, R. G. (2016, July). Very deep learning for ship discrimination in synthetic aperture radar imagery. In *Geoscience and Remote Sensing Symposium (IGARSS), 2016 IEEE International* (pp. 104-107). IEEE.
- Shay, L. K., Lentz, S. J., Graber, H. C., & Haus, B. K. (1998). Current structure variations detected by high-frequency radar and vector-measuring current meters. *Journal of Atmospheric and Oceanic Technology*, 15(1), 237-256.
- Suchandt, S., Runge, H., Breit, H., Steinbrecher, U., Kotenkov, A., & Balss, U. (2010). Automatic extraction of traffic flows using TerraSAR-X along-track interferometry. *IEEE Transactions on Geoscience and Remote Sensing*, 48(2),

807-819.

Suchandt, S., & Runge, H. (2012, July). First results of TanDEM-X along-track interferometry. In *Geoscience and Remote Sensing Symposium (IGARSS), 2012 IEEE International* (pp. 1908-1911). IEEE.

Suchandt, S., & Runge, H. (2015). Ocean surface observations using the TanDEM-X satellite formation. *IEEE Journal of Selected Topics in Applied Earth Observations and Remote Sensing*, 8(11), 5096-5105.

Szegedy, C., Vanhoucke, V., Ioffe, S., Shlens, J., & Wojna, Z. (2016). Rethinking the inception architecture for computer vision. In *Proceedings of the IEEE Conference on Computer Vision and Pattern Recognition* (pp. 2818-2826).

Vachon, P. W., Campbell, J. W. M., Bjerkelund, C. A., Dobson, F. W., & Rey, M. T. (1997). Ship detection by the RADARSAT SAR: Validation of detection model predictions. *Canadian Journal of Remote Sensing*, 23(1), 48-59.

van der Kooij, M., Hughes, W., & Sato, S. (2001). Doppler current velocity measurements: a new dimension to spaceborne data. Unpublished manuscript.

Wong, F., & Cumming, I. G. (1996). A combined SAR Doppler centroid estimation scheme based upon signal phase. *IEEE Transactions on Geoscience and Remote Sensing*, 34(3), 696-707.

Yang, J., & Zhang, Y. (2015). Analysis on the Azimuth Shift of a Moving Target in SAR Image. *Progress In Electromagnetics Research*, 42, 121-134.

- Young, I. R. (2006). Directional spectra of hurricane wind waves. *Journal of Geophysical Research: Oceans*, 111(C8).
- Zebker, H. A., & Goldstein, R. M. (1986). Topographic mapping from interferometric synthetic aperture radar observations. *Journal of Geophysical Research: Solid Earth*, 91(B5), 4993-4999.
- Zhang, L., Zhang, L., & Du, B. (2016). Deep learning for remote sensing data: A technical tutorial on the state of the art. *IEEE Geoscience and Remote Sensing Magazine*, 4(2), 22-40.
- Zilman, G., Zapolski, A., & Marom, M. (2004). The speed and beam of a ship from its wake's SAR images. *IEEE Transactions on Geoscience and Remote Sensing*, 42(10), 2335-2343.

국문요약

합성개구레이다(SAR)의 도플러 파라미터 추정은 속도 추출을 위한 가장 효과적인 도구 중 하나이다. 시야 방향의 속도를 추정하는 원리는 SAR 자료로부터 추출된 도플러 변이(Doppler shift)를 활용하는 것이다. 도플러 변이는 센서와 지표면 사이의 상대적인 움직임에 의해 발생한다. 다양한 지구상의 움직임은 대상체의 속도 범위에 맞게 속도를 추정하기 위하여 도플러 파라미터 추정 방법을 통해 해양, 지질, 도심, 군사 등의 연구 분야에서 활용이 가능하다. 다양한 SAR 자료 레벨과 그에 맞는 도플러 파라미터 추정 기법에 따라서 광범위한 대상체와 인공 대상체의 속도 추출이 가능하다. 본 논문에서는 SAR 원시 자료를 이용하여 해양 표면과 같은 광범위한 대상체의 속도를 추출하는 연구와, SAR SLC 자료를 이용하여 선박과 같은 움직임은 인공 대상체의 속도를 추출하는 연구를 각각 수행하였다.

1. RADARSAT-1 ScanSAR 원시 자료의 도플러 파라미터를 이용하여 해양 표면의 속도를 추출하였다. 해양 표면 속도는 측정된 도플러 중심주파수와 예측된 도플러 중심주파수 사이의 도플러 변이를 추출함으로써 추정이 가능하다. 대상체가 움직이지 않는다고

가정하고 위성의 궤도, 빔 포인팅 방향, 위성 비행자세 및 지구 자전 효과 등이 고려되어 향상된 기하학 파라미터를 기반으로 계산된다. Slant range, look angle, hour angle 등의 향상된 기하학 파라미터를 기반으로 기하학 모델을 사용하였다. 추가적으로, RADARSAT-1의 부정확한 비행자세 정보로 인한 오차를 보정하기 위하여 비행 자세 조정 알고리즘(attitude control algorithm)과 global fitting 방법을 포함한 iterative fitting 방법을 적용하였다. 반면에, 실제 움직이는 대상체는 수신된 SAR 원시 자료의 위상 정보를 ScanSAR 자료에 적합하게 조정된 평균교차상관계수(Average cross correlation coefficient; ACCC) 방법을 적용하여 측정된 도플러 중심주파수 계산이 가능하다. RADARSAT-1 ScanSAR 도플러 중심주파수 추정 기법(Doppler centroid measurements)을 통해 열대성 저기압(태풍, 허리케인, 사이클론 등)에 반응하는 해양 표면의 속도를 추출하였다. 5개의 다른 열대성 저기압(Typhoon Xangsane, Hurricane Dean, Hurricane Ivan, Hurricane Lili, Hurricane Kyle)과 연속적으로 획득한 허리케인(Hurricane Lili and Hurricane Kyle)을 선정하여 해양 표면 속도를 추출하였고, 표류 뜰개(drifting buoy)의 이동 궤적을 통해 측정된 해류 분석 결과와 비교하였다. 비교한 결과 일반적인 해류와는 달리 바람이 강한 열대성 저기압에서의 해양 표면 속도는 표

층 해류의 속도와 매우 유사하게 관측되었다. 본 연구는 다양하고 연속적인 열대성 저기압에 반응하는 해양 표면 속도를 추출하기 위하여 인공위성 RADARSAT-1 ScanSAR 원시 자료를 이용하여 도플러 중심주파수 추정 기법을 활용한 최초의 연구이다.

2. TanDEM-X SLC 영상에 관측된 선박과 항적 사이의 선박과 항적 사이의 도플러 변이로 인해 발생하는 방위각 변위 (azimuth offset) 를 이용하여 이동하는 선박의 속도를 추출하였다. 선박과 항적 사이의 방위각 변위는 후방 산란 신호의 도플러 변이 효과에 비례하므로 움직이는 대상체의 시야 방향 속도와 관련된다. 이때 선박과 항적이 각각 포함된 subset 자료의 자동 선정을 위해, 딥 러닝 학습 기법 중 Convolutional Neural Networks (CNN) 기법을 사용하여 SAR SLC 영상으로부터 선박과 항적을 각각 탐지한다. 탐지된 항적의 subset 자료는 edge 필터와 라돈 변환(Radon Transform)을 통해 두 선형 성분으로 나타낼 수 있고, 두 선형 성분의 교차점이 원래의 선박 위치라고 판단할 수 있다. 이 두 선형 성분의 교차점과 식별된 선박 사이의 방위 방향으로의 변위 거리를 계산하여 선박의 속도를 추정하였다. 추가적으로, 도플러 변이로 인해 발생하는 Along-track interferometry (ATI) 기법을

통해 움직이는 선박의 속도도 추출하였다. 연구 지역은 대한해협으로 선정하였으며, 당시 TanDEM-X 영상에 관측된 선박을 탐지하고 속도를 추출하였다. 상대적으로 느린 선박의 속도로 인해 탐지된 항적의 개수가 작긴 했지만, AIS(자동항법시스템)와 비교해보았을 때 선박과 항적은 높은 탐지 정확도를 보여주었다. 탐지된 선박과 항적 사이의 방위각 변위를 이용한 선박 속도와 ATI 위상 정보를 이용하여 추출된 선박의 속도, AIS로 획득된 선박 속도 자료를 각각 비교하였다. 방위각 변위 방법을 통한 선박 속도 추출 기법이 상대적으로 높은 정확도의 선박 속도 추출이 가능하였다. TanDEM-X ATI로 추출된 선박 속도는 선박 구조물 높이로 인한 XTI 성분이 완벽하게 제거되지 않았기 때문에 어느정도 오차를 포함하였다. 본 연구는 딥 러닝 기법을 통해 선박뿐만 아니라 항적까지도 탐지를 하였고, 자동으로 subset 자료를 생성하였다. 항적만 탐지된 자료는 edge 필터와 라돈 변환을 통해 subpixel 해상도의 방위 방위각 변위 거리를 측정하여 정밀한 선박의 속도로 변환할 수 있었다.

따라서 본 연구에서, 도플러 중심주파수 측정 방법, 방위각 변위, ATI 등을 이용한 SAR 도플러 파라미터 추정 연구를 통해 표층 해류

와 선박 속도 등의 다양한 활용 분야의 움직이는 대상체의 속도 추출 기법의 새로운 가능성을 제시하였다.

주요어: 합성개구레이다, 도플러 중심주파수 추정 기법, 방위각 변위 기법, 표층 해류, 선박 속도, Along-track interferometry SAR,